



Raymond P. Mariella, Jr., Center Leader

The mission of the Microtechnology Center at Lawrence Livermore National Laboratory (LLNL) is to invent, develop, and apply microtechnologies in conjunction with programs in global security, global ecology, and bioscience.

Our capabilities cover materials, fabrication, devices, instruments, or systems that require micro-fabricated components, including micro-electro-mechanical systems (MEMS), electronics, photonics, microstructures, and microactuators. All of our microtechnology work revolves around our micro-fabrication facility, and is driven principally by the applications of our internal programs, and to a lesser extent, by external applications. For both of these we must have multidisciplinary teams to deliver complete solutions to the problems.

The Microtechnology Center continued to grow in FY-98. Its more than 60 people have training in electronics engineering, mechanical engineering, chemical engineering, chemistry, physics, and the biosciences. Our recent successes in analytical instrumentation reflect our broad, multidisciplinary base and the cross-fertilization that results from personnel sharing their capabilities and ideas with each other.

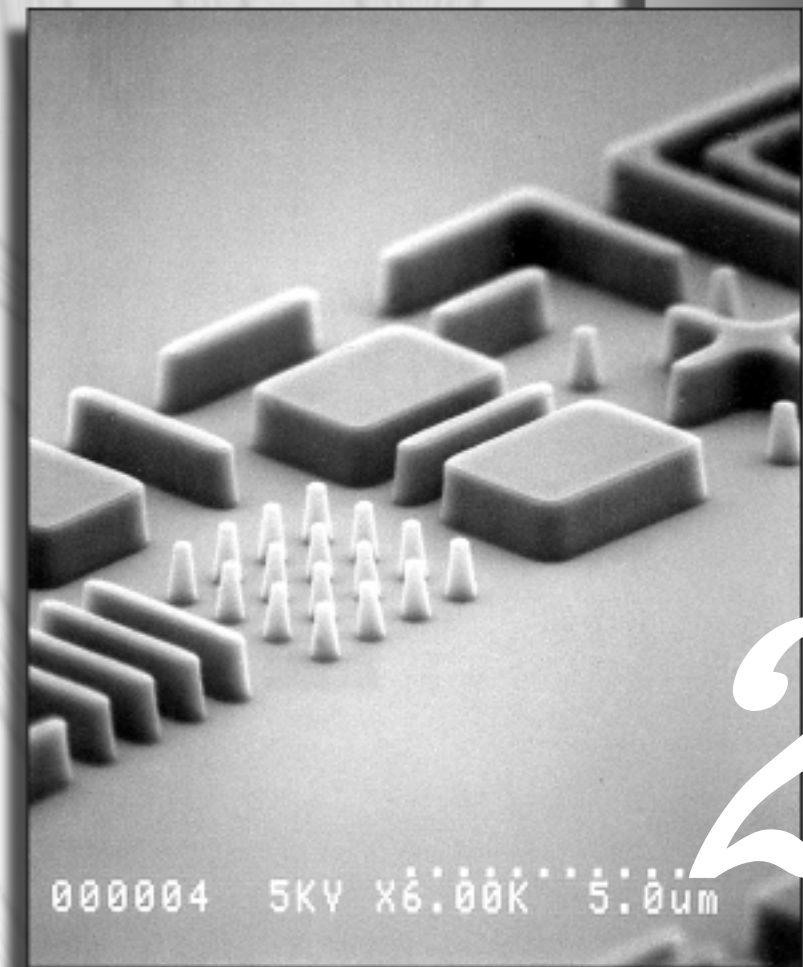
We continue to show a very high rate of return on investment. Over the last year, with a total budget of more than \$15M, including approximately \$0.6M of technology-base projects, we have successfully performed collaborations with industry, and have achieved considerable national recognition. We have had success in our on-going instrumentation project, developing both polymerase chain reaction (PCR) assays and instrumentation, supported by the Defense Intelligence Agency.

In January of 1998, we took our latest PCR instrument to the Joint Field Trials IV (JFT IV) in Dugway, Utah, for the open competition and demonstrated the highest sensitivity ever recorded there for detection of the plague simulant (*Erwinia herbicola*). Our microtechnology project on the fabrication of facets for GaN lasers has also shown excellent results.

As the applications for microtechnology grow, we continue to perform the technology-base activities that are needed to fulfill the needs of our LLNL and external partners and stay in a leadership position, both nationally and world-wide.

Overall, the numerous small investments in microtechnology have paid off this year in 1) outstanding results at JFT IV with the LLNL PCR instrument; 2) the highest performance hand-held gas chromatograph built, including microfabricated injector, column, and detector; 3) an LLNL electrophoresis system with etched/bonded plates containing 384 channels; 4) \$1M in DARPA funding for dielectrophoresis technology; 5) a \$1.7M CRADA: a medical catheter device to release embolic coils into cerebral aneurysms that uses laser light for release and detection; 6) projects for optical interconnects in partnership with the Photonics Program, resulting in significant demonstration of multiple-wavelengths carried per fiber; 7) highly visible multi-million-dollar CRADA with semiconductor businesses for EUV lithography; and 8) collaboration with the University of California, Santa Barbara, on high-performance laser facets for GaN and demonstration of an advanced process in laser-based doping of GaN.

# Center for Microtechnology



2

## 2. Center for Microtechnology

### Overview

*Raymond P. Mariella, Jr., Center Leader*

### Disposable Microfluidic Biological Sample Preparation System

*Robin R. Miles, Daniel L. Schumann, Kelye A. Allen, Jim A. Butler, and Kerry A. Bettencourt .....2-1*

### Sub-Micron Lithography with a 5X Stepper

*Dino R. Ciarlo and Benjamin P. Law .....2-5*

### Advanced Packaging for Wireless Microsensor Modules

*Abraham P. Lee, Charles F. McConaghy, Jimmy C. Trevino, Leslie M. Jones, and Jonathan Simon.....2-7*

### Radio Frequency Technology for Wireless Microsensor Modules

*Charles F. McConaghy, Abraham P. Lee, Charles Chien, Chris Deng, and Igor Elgorria .....2-11*

### Ultra-High-Speed Analog-to-Digital Conversion Technology

*Mark E. Lowry, Ronald E. Haigh, and Charles F. McConaghy .....2-13*

### HV Photovoltaics

*Karla G. Hagans and Ronald E. Haigh.....2-17*

### Lattice Boltzmann Simulation of Complex Fluid Flows

*David S. Clague .....2-19*

### Micro-Electromechanical Systems (MEMS) for Characterization of Plastic-Bonded Explosives

*Jeffrey D. Morse, Dino R. Ciarlo, Scott E. Groves, Diane J. Chinn, Mehdi Balooch, and Mark J. LaChappel.....2-23*

### Micro-Electromechanical-Systems-(MEMS)-Based Fuel Cell Technology

*Jeffrey D. Morse, Robert T. Graff, Alan F. Jankowski, and Jeffrey P. Hayes .....2-27*

### High-Power GaN Microwave Device Technology

*Glenn A. Meyer, Gregory A. Cooper, Stacy L. Lehew, Thomas W. Sigmon, Daniel Toet, Steven DenBaars, and Umesh Mishra .....2-31*

### Glass Etching

*Harold Ackler and Stefan P. Swierkowski.....2-37*

### Micro-Electromechanical Systems Foundry Interface

*Michael D. Pocha .....2-41*

### A Hydrogel-Actuated Implantable Sensor

*Amy W. Wang, Abraham P. Lee, Charles F. McConaghy, Christopher B. Darrow, Aleksandr Gilman, Stephen M. Lane, and Joe H. Satcher, Jr. ....2-45*

### Lambda Connect: Multi-Wavelength Technologies for Ultrascale Computing

*Robert J. Deri, Michael C. Larson, Michael D. Pocha, and Mark E. Lowry.....2-49*

# isposable Microfluidic Biological Sample Preparation System

**Robin R. Miles**

*Electronics Engineering Technologies Division  
Electronics Engineering*

**Daniel L. Schumann, Kelye A. Allen, and Jim A. Butler**

*Manufacturing and Materials Engineering Division  
Mechanical Engineering*

**Kerry A. Bettencourt**

*Materials Science and Technology Division  
Chemistry and Materials Science*

We have fabricated plastic microfluidic devices to provide an inexpensive flow path for biological applications. External actuation was used for valving, pumping, and mixing functions. The advantages to this system over alternative microfluidic approaches are that it provides isolation of the biological material from actuators, reduces material compatibility concerns and system cost, and minimizes dead volume.

## Introduction

The purpose of this project was to develop a microfluidic circuit based on thin film plastic. Fluidic channels and plenums were formed using thin film plastic such that they could be manipulated externally to provide valving, pumping, and mixing functions, as shown in **Fig. 1**. The device can be used in either a disposable or a semi-fixed system.

The chief advantage to such a system is that it provides isolation of the biological fluid from the actuation device. Low-power actuators, such as piezoelectric or electrostatic actuators, are generally incompatible with fluid environments. High-work actuators, such as thermal actuators, require significant increases in power when in contact with fluids.

Other advantages to this system over alternative microfluidic approaches include the use of a single material to reduce material compatibility concerns, reduce system cost, and minimize dead volume.

## Progress

The primary focus of this effort was to develop a fabrication process for defining and sealing the plastic sheets. A second effort was to develop an

external pneumatic actuator for the system to provide valving, pumping, and mixing operations.

## Forming the Plastic Sheet

Forming and bonding the plastic sheets proved to be a difficult task. Our technique for manufacturing the plastic device was to first pre-form the cavities on each half of the structure, then bond the two halves together to make the final structure. We developed several techniques to form the plastic structure including heat-staking, laser welding, and molding. Stiff plastics such as polypropylene and polyethylene were first embossed to define the tubing and plenum areas of the structure, then laser welded to a second sheet of plastic to complete the structure. Elastomeric materials such as metallocene and silicone were molded or heat-staked.

**Thermal Heat-Staking.** Several outside vendors were contacted to provide heat-staking fixtures for fabricating the plastic structures. One vendor built a fixture for bonding pre-embossed polypropylene sheets. Unfortunately, their fabrication technique proved unsuccessful as they melted the entire plastic structure into one big lump. A second vendor successfully bonded two sheets of metallocene in

the desired configuration to provide for the desired internal tubes and plenums. The bonds were capable of withstanding 10 psi internal pressure.

**Laser Welding.** A CO<sub>2</sub> laser was used successfully to thermally weld the two halves of the plastic structure. **Figure 2** shows devices that were bonded together using this technique. Maintaining intimate contact between the plastic sheets was the primary challenge for laser welding these structures. For flat sheets, we used a vacuum platform to suction the work together and cut the top sheet larger than the bottom sheet. For embossed sections, we made nesting fixtures out of acrylic. We adjusted the height and spread of the beam to get reasonable welds. We were able to produce welds which held to internal pressures of 15 psi. However, we were not able to get within 0.02 in. of the edge of the raised embossed plastic because the two plastic films could not be reliably held together near that interface. Also, we could only weld a flat sheet with one embossed side, or two sheets that were embossed simultaneously and in the same direction. Later welds performed for a PCR sample preparation system were not leak-free due to the difficulty of controlling the very low energy density level of the available laser.

**Silicone Molding.** We turned to silicone for this application because of the increased manufacturability of the structures and the higher probability for obtaining good valve shut-off. We used etched silicon wafers to form molds into which we poured a two part, heat-cured silicone. We used both Sylgard 184 and Sylgard 186. We used two mirror-imaged molds

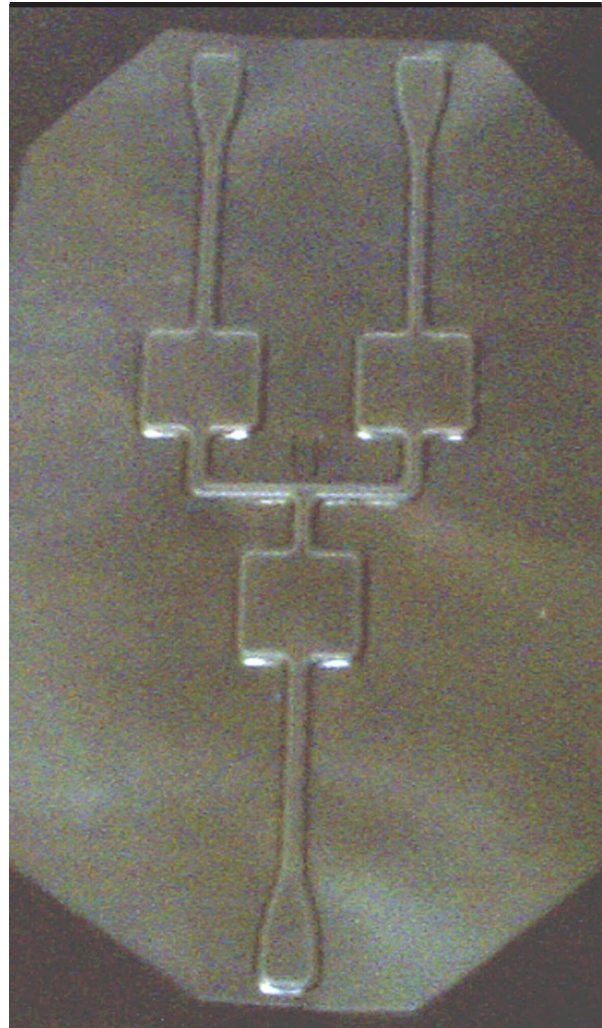
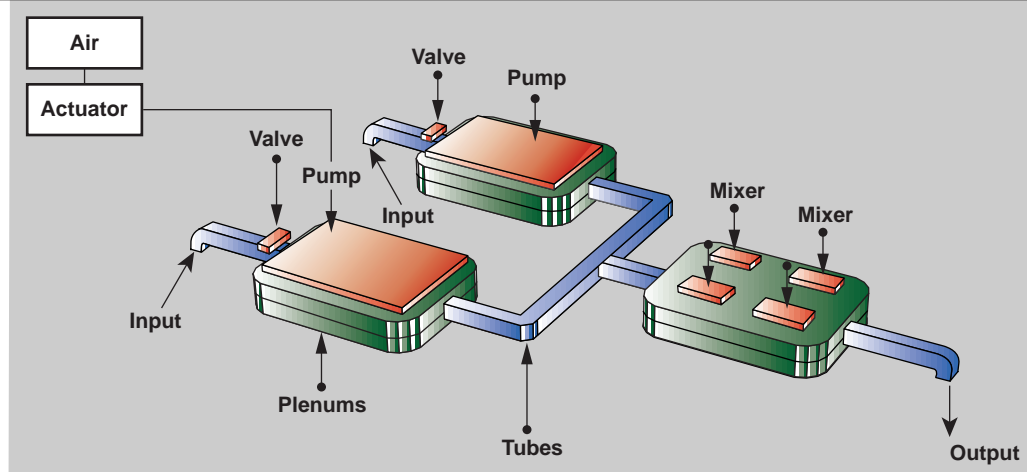
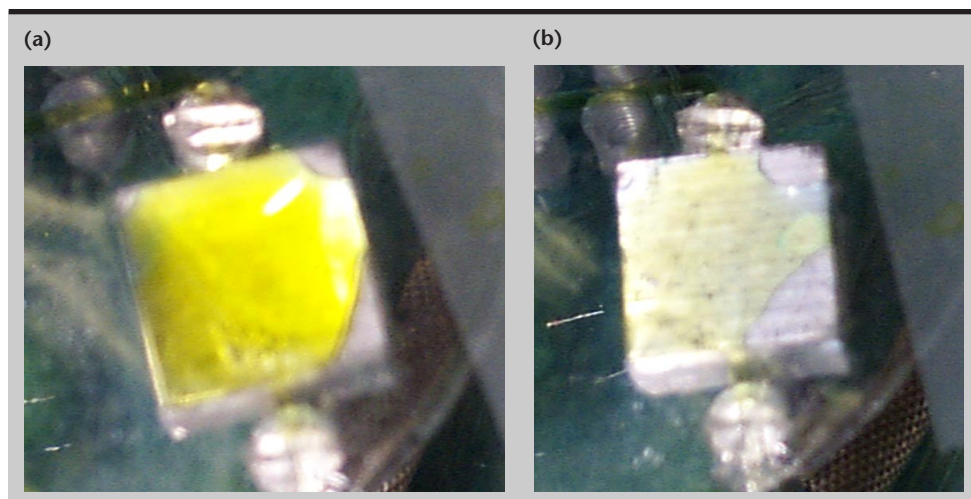


Figure 2. Embossed and laser-welded plastic sheet.

Figure 1. Formed plastic structure with external actuation.







*Figure 3. Pumping actuation on silicone chamber using pneumatic cylinder actuator.*

to form two halves of the final structure. We cured these halves, removed them from the mold, then painted on an additional amount of the silicone to act as a glue between the two halves. Thus, the entire mold is made from just one material.

The Sylgard 186 is tougher, more tear-resistant, and has better adhesion than the Sylgard 184, but is much more viscous and sticks to the mold too well and is, therefore, difficult to use. However, we were able to make devices that could withstand a 35-psi internal pressure before delamination of the layers occurred.

**Interconnects.** Interconnecting the device to the outside world proved difficult. For the flat sheets, we designed a flared section that could be mated to a standard leur fitting. However, these leaked a little when used directly and needed sealant to hold. For the silicone structures, we used the silicone as the sealant for tubes that were inserted into the molded device. The best results were obtained using PEEK tubing, and acceptable results with silicone tubing. Tygon tubing tended to harden up and tear the molded device. Good surface preparation of the tubing was required for a good seal.

### Pneumatic Actuation

Pneumatic actuation was used to provide the valving, pumping, and mixing functions of the fluidic circuit. One method of providing pneumatic actuation was to use silicone-molded buttons that were held in an aluminum clamped fixture, which created a silicone membrane that could be distended using air driven through standard pneumatic fittings. The silicone rubber was very flexible, and this method worked well, particularly for pumping.

The smaller buttons used for valving required a higher pressure. We found that complete shut-off of


the flow required a channel depth on the order of 100  $\mu\text{m}$  for the silicone molded devices, and zero gap for the welded plastic sheet. A second method for providing pneumatic actuation is to use off-the-shelf pneumatic cylinders attached to an aluminum plate for providing force against the plastic structure. Pumping and mixing can be accomplished using pneumatic cylinders. Additional force for valving was obtained by replacing the aluminum plate at the end of the pneumatic cylinder with a 0.010-in.-wide shim.

We found that we could also spin Sylgard 184 over silicon nitride windows formed by etching a silicon wafer to make silicone membrane actuators that may be more compatible with micromachined devices. The silicon nitride could be removed by a post-cure dry etch.

### System Results

We were able to demonstrate the functions of pumping, valving, and mixing using these devices. Pumping is shown in **Fig. 3**. The fluid is forced from the silicone chamber using an external pneumatic plunger.

### Future Work

We are using this technology in two other applications, a sample preparation system for the autonomous point detector program, and a hand-held PCR system. The heat-staked metallocene structures are the most cost-effective structures and will serve as the basis for the applications of this technology. We are working to replace the pneumatic actuators with low-power piezoelectric actuators and manually driven cam devices to make this device more attractive for portable applications. 





# ub-Micron Lithography with a 5X Stepper

**Dino R. Ciarlo and Benjamin P. Law**  
*Electronics Engineering Technologies Division*  
*Electronics Engineering*

This year we installed a lithography system capable of printing sub-micron features onto silicon wafers. The system is a refurbished GCA DSW, Model 8500, which is an i-line system (365 nm), capable of printing 0.7- $\mu$ m features anywhere within a 16-mm field of view. This system is now operational in the Microtechnology Center (MTC) at the Lawrence Livermore National Laboratory (LLNL).

## Introduction

We continue to get requests for lithography with feature sizes  $< 2 \mu\text{m}$ . From time to time, there are even requests for sub-micron images. The existing remote wireless sensors and adaptive optics projects are designing devices based on 2- $\mu$ m rules, while the giant magneto-resistive (GMR) sensor project uses sub-micron features. In addition, we get requests for Fresnel zone plates and pinhole arrays with sub-micron feature sizes.

The contact printers in LLNL's MTC can be used down to 2  $\mu\text{m}$ , with increasing difficulty because of diffraction effects. A new state-of-the-art projection lithography system with sub-micron printing capability can cost more than \$5M. Fortunately, there is an industry dealing in used, refurbished equipment with adequate capability. We accepted delivery of a GCA DSW Model 8500 in January 1998. It is now operational in the MTC. The system is ten years old, cost \$255K, and has been refurbished to perform to its original specifications, which allows the printing of 0.7- $\mu$ m features.

## Progress

We spent several months working with the vendor to install and learn to operate this system. It is a 5X reduction system, which means the photomasks need to be designed at five times the size of the features to be printed on the silicon wafer. The reduction lens is referred to as a T1635P, which means it has a 16-mm circular field of view with a numerical aperture of 0.35. This allows the printing of 0.7- $\mu$ m features in 1- $\mu$ m-thick resist, anywhere within the 16-mm field of view. The illumination

source is a 1000-W mercury lamp which provides i-line illumination (365 nm). Typical exposure times for 1- $\mu$ m-thick resist is 0.5 s. The system has its own environmental control chamber and atmospheric control system (ACS) to regulate temperature, pressure, and humidity.

This system has many automated features that are used to optimize its performance. For example:

1. RMS—Reticle Management System, used to select from 10 reticle stores in a rack. Each reticle is labeled with a bar code.
2. AWH—Automatic Wafer Handler, automatically loads and unloads 100-mm-diameter silicon wafers from cassette holders.
3. AFII—Autofocus System, automatically maintains best focus as the wafer is stepped from die to die.
4. AWA—Automatic Wafer Alignment, does the initial global alignment of the reticle to the wafer.
5. DFAS—Dark Field Alignment System, used for the final die-by-die alignment of the reticle to the wafer. Initial alignment is accomplished by a laser interferometer-controlled x-y stage. Final alignment is better than  $\pm 0.15 \mu\text{m}$ .

To properly use the automatic sub-systems, the main system must first be set up to be within their "capture" range. This is done during initialization of the system. The initialization parameters are stored in the MODE program for system operation.

Also, special targets need to be placed on the reticles for these automatic sub-systems to operate. For example, the AWA and DFAS sub-systems both need special targets to be placed on the reticles, in the proper position.



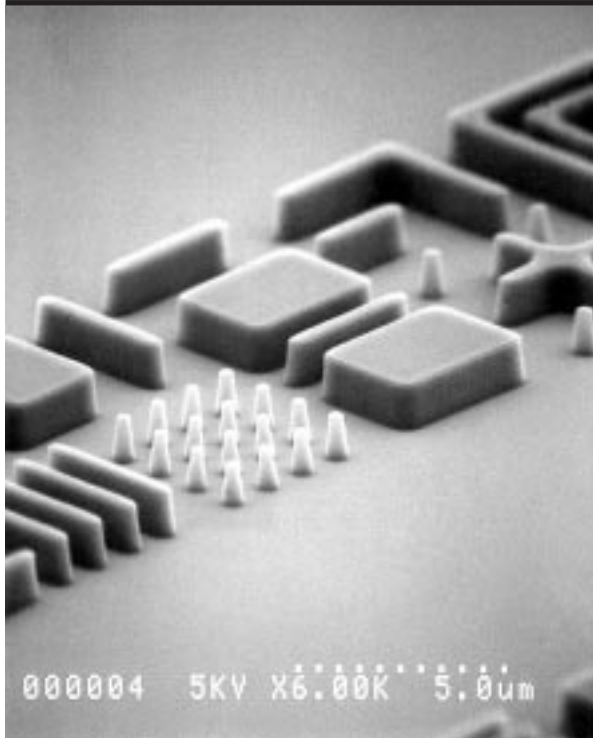


*Figure 1. SEM image of features printed in 1- $\mu$ m-thick positive resist. The small pedestals have a diameter of 0.5  $\mu$ m.*

**Figures 1** and **2** show SEMs of resist images printed in 1- $\mu$ m-thick JSR 500 positive resist. The smallest pedestals in **Fig. 1** have a diameter of 0.5  $\mu$ m. In **Fig. 2** are pedestals with lateral features of 1.4  $\mu$ m by 1.4  $\mu$ m. The sidewalls are nearly vertical.


### Future Work

This 5X reduction system is now being used for several LLNL projects. We continue to learn how to operate the system and are becoming more comfortable with its capabilities. The system is optimized to use 100-mm-diameter silicon wafers

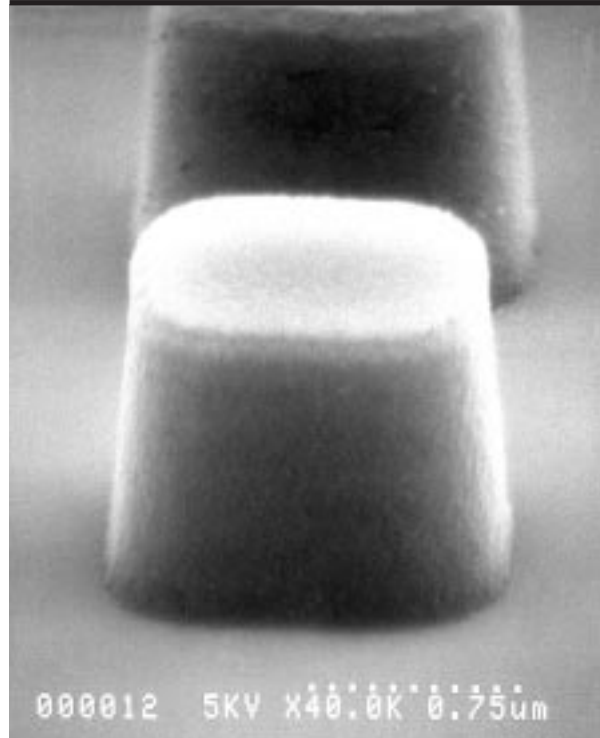


*Figure 2. SEM image of a square resist pedestal. Resist thickness is 1  $\mu$ m. Area of pedestal is 1.4  $\mu$ m by 1.4  $\mu$ m.*

that are 500  $\mu$ m thick. We recently had a project that is using 100-mm-diameter wafers only 375  $\mu$ m thick. This required a rather difficult manual adjustment of the optical column to focus onto the thinner wafers. Most likely, we will be getting other requests to print on “non-standard” substrates. The computer that controls the system is rather dated and is not very user-friendly, but we are learning.

Finally, there are now only three members of the MTC trained to operate this system, but we expect to add two to three more to this list of operators in the future. 

# Advanced Packaging for Wireless Microsensor Modules

**Abraham P. Lee, Charles F. McConaghy, Jimmy C. Trevino,  
and Leslie M. Jones**

*Electronics Engineering Technologies Division  
Electronics Engineering*

**Jonathan Simon**

*New Technologies Engineering Division  
Mechanical Engineering*

We have developed packaging technologies to integrate the components of wireless sensing modules such as MEMS microsensors, sensor electronics, modems, RF transceivers, and RF electronics, all of which may ultimately be on individual dies.

## Introduction

A wireless microsensor module consists of four basic parts:

1. sensor—could be a low-g ( $\mu\text{g}$ ) accelerometer. The sensor makes use of both bulk and surface micromachining.
2. interface electronics—to convert the signal from the sensor to a usable voltage. The interface electronics drive an A/D converter, which in turn interfaces to the modem.
3. modem electronics—the electronics that take care of some portion of the protocol, as well as producing the spread spectrum codes to drive (transmit data) or decode (receive data) the RF portion of the module.
4. RF section—the mixers, oscillators, amplifiers, and antenna switch. This section is the interface between the modem and the antenna.

To integrate these dissimilarly processed parts into a compact form factor, it is necessary to develop advanced packaging processes. We have chosen a microaccelerometer sensor to demonstrate a wireless module and establish the integration technologies.

The next generation of defense and intelligence activities requires covert large-area sensing networks for extended periods of time (one month to one year). Current micro-electromechanical systems

(MEMS) technologies can enable only a point detection device without communications between multiple nodes. Wireless technologies are not self-sufficient without physical transduction capabilities through MEMS. The combination of the two is of limited use if it isn't covert, or close to covert. Although there are many microsensors being developed commercially and in academia, none are integrable with wireless communications platforms to enable network sensing.

The challenge lies in the integration of different chips in a compact form, which requires techniques to ensure compatibility of process and signal interfaces. The engineering capabilities supporting the Microtechnology Center (MTC) at Lawrence Livermore National Laboratory (LLNL) have interdisciplinary expertise in 1) MEMS-based microsensor design; 2) MEMS electronics packaging; 3) MEMS electronics sensing design, deep reactive ion etching (DRIE) capability (a key to integrating micromachining technologies in a compact form); and 4) programmatic applications requiring a systems approach and allowing the generation of a standard protocol.

Integration of the numerous parts of the module will be designed from the systems level to ensure miniaturization, compatibility in electronic interconnect and compatibility in different processing sequences.

Most other researchers are working on singular aspects of the problem, such as the wireless and MEMS technologies. Challenges to combine the state of the art in MEMS and wireless communications is a unique opportunity, bringing together expertise in electronics and mechanical engineering, chemistry and materials science, and nonproliferation control.

The technology developed by this project will directly enhance core competencies in the MTC since it will enable the integration of micromachining technologies for many applications.

While there are many researchers in the field, LLNL can distinguish itself as the leader in technology integration with advanced packaging of wireless

components, large quantity sensor networks, and advanced MEMS electronics packaging. It also allows the opportunity for LLNL to set the standards and protocols for wireless microsensor modules and networks.

For the remote sensing needs that are increasingly important in this post-cold-war era, this project could have a significant effect on monitoring treaties and combatting urban warfare. It affects the capability to maintain world peace and national security. The State of California could benefit from border control technologies developed from this project. This project is in direct alignment with LLNL's mission of global security.

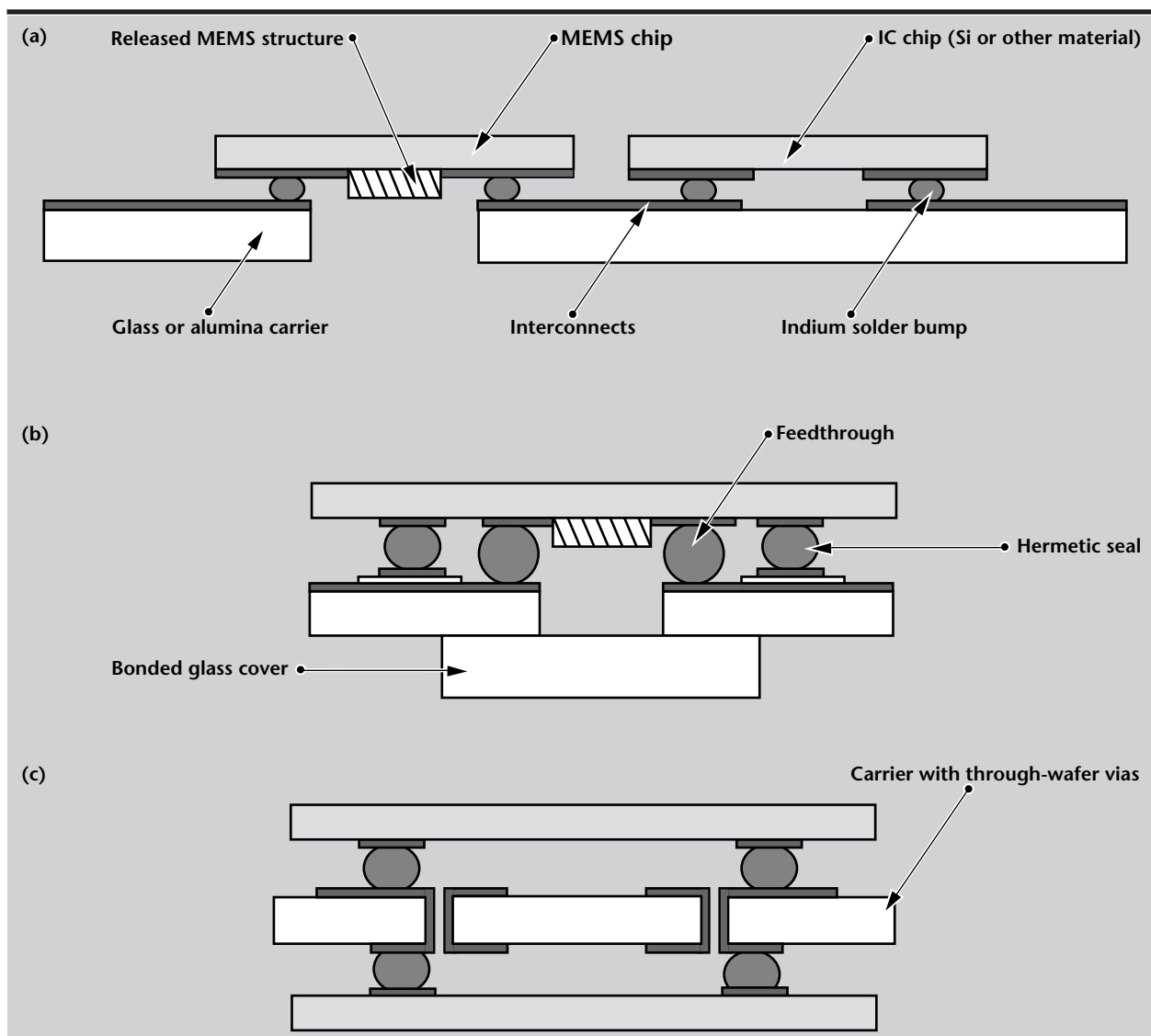


Figure 1. MEMS-integrated MCM packaging scheme.

## Progress

### Integration of Wireless Microsensor Module

We have developed packaging technologies to integrate the components of wireless sensing modules such as MEMS microsensors, sensor electronics, modems, RF transceivers, and RF electronics, all of which may ultimately be on individual dies.

There are several important constraints to the design:

1. Chips may be fabricated from different materials and processes, such as Si and GaAs.
2. Chips may be of largely varying size from  $2\text{ mm} \times 2\text{ mm}$ , to  $1\text{ cm} \times 1\text{ cm}$ .
3. MEMS sensors may require vacuum, fluid, or gas environments.
4. Post-processing of the chips should be minimal.
5. The approach is flexible.

We have opted for a Flip-Chip Multi-Chip Module (MCM) approach. In such a design, the individual chips are flipped over and bonded to a carrier, rather than interconnected using wire bonds. The hybrid package can then be further encapsulated or repackaged as necessary.

**Figure 1a** shows a glass (fused silica or Corning 7740) or alumina carrier with patterned interconnects and electro-deposited indium solder bumps. All the processing is done on the carrier wafer to ensure compatibility and minimize the handling of the various dies.

A variety of chips can then be flip-chip-bonded to the carrier. In this case, a recess for the MEMS device has been milled into the carrier. This recess can serve as an attachment point for fluid or gas interconnects, or as in **Fig. 1b**, the indium may also be used to seal the MEMS die into a vacuum reservoir or other filled reservoir.

In the case of extremely space-constrained systems, addition of through-wafer vias (**Fig. 1c**) to the carrier effectively doubles the packaging density.

A fabrication process flow for a carrier wafer with no vias is shown in **Fig. 2**. A carrier wafer of glass (fused silica or Corning 7740) is coated with a metal seed layer of  $500\text{ \AA}$  Ni/ $2000\text{ \AA}$  Au/ $100\text{ \AA}$  Ti. The gold acts as the primary conductor, while the titanium acts as an adhesion layer, and the nickel acts as a barrier to keep the plated indium from diffusing into the gold.

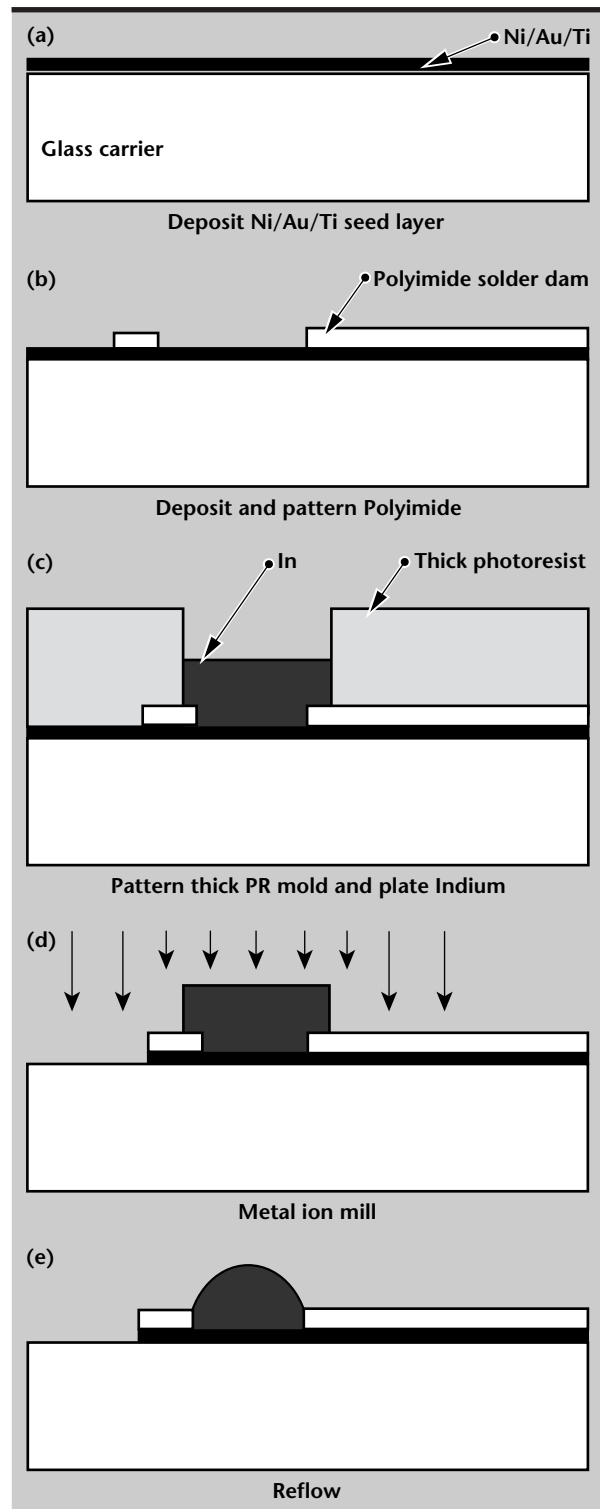
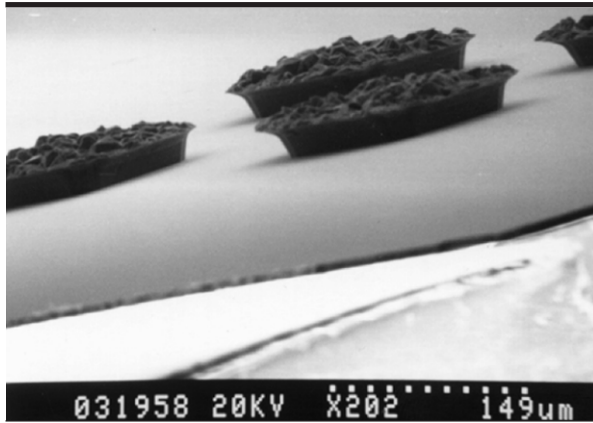



Figure 2. Process flow for carrier wafer traces and indium solder bumps.



*Figure 3. SEM of ~35- $\mu$ m-tall electroplated indium bumps before reflow.*

In the first mask step, a polyimide layer is patterned which will be used both as a solder dam for the indium and to define the traces. In the second mask step, a thick photoresist is spun onto the wafer and patterned to make a mold for indium plating.

After indium plating ( $\sim 50\text{ }\mu\text{m}$ ), the photoresist is stripped, and the parts are ion-milled to pattern the traces. The indium is then reflowed in an inert environment to form uniform bumps. **Figure 3** shows  $35\text{-}\mu\text{m}$ -tall indium bumps before reflow. 

# **R**adio Frequency (RF) Technology for Wireless Microsensor Modules

**Charles F. McConaghy and Abraham P. Lee**

*Electronics Engineering Technologies Division  
Electronics Engineering*

**Charles Chien, Chris Deng, and Igor Elgorria**

*University of California, Los Angeles*

We have developed a small, low-power RF link for connecting sensors to a central node. The link is in the 900-MHz ISM band and uses spread spectrum technology, as well as time division multiple access, to accommodate multiple sensor modules. This was a joint project with researchers at the University of California, Los Angeles (UCLA). The modem and RF technology developed at UCLA is being incorporated into a Lawrence Livermore National Laboratory wireless sensor package.

## **Introduction**

Networks of low-power wireless sensors are envisioned to accommodate future sensor needs in the field. Such packages should not only include sensors, such as a seismic or bio-sensor, but also the means to transmit this information to some distant monitoring point. These sensors should be very low power and small in both size and weight to allow for ease in deployment. The communication distance of any module is about 30 to 100 m, and the RF power is 1 mW. However, networks of these modules can be assembled to cover much longer distances. The module being constructed this year is a cube 2 in. on a side. The RF components occupy about one third of the volume, the batteries and sensor occupy the remaining volume.


## **Progress**

The RF section consists of a modem which is used to both modulate and demodulate the digital data onto and from a 900-MHz RF carrier that has been implemented with a field-programmable gate array (FPGA). In addition, on the sensor end of the RF link, the modem is also used to read the A/D converter that digitizes the sensor output. An additional operation of the FPGA is the superposition of a pseudo-random code on the data at transmit, and the removal of this code upon reception. Besides the

modem, the necessary RF circuits, which either up-convert on transmission or down-convert on reception, the modem signals have been implemented on a pc board that is 2 in. square. These circuits were designed and built during FY-98.

A time division protocol has also been implemented which allows each sensor module to completely power its RF circuitry off except when needed. In low-power applications, even the receiver can cause a significant battery drain. The time division protocol allows each sensor module to power up its RF circuitry for 260 ms and then be off for about 2 s to save power. There is a sophisticated resynchronization process that occurs periodically to keep the clocks in the sensor module in sync with the base station that is interrogating the modules.

## **Future Work**

Future work requires that we make even smaller and lower power RF circuitry, such that smaller batteries can be used for longer periods of deployment. In addition, the overall sensor module needs to fit a package that is about one cubic inch in volume, which means that the RF circuitry needs to be decreased in size. This will be achieved by using applications-specific integrated circuits (ASICs) rather than FPGAs, and RF chips with more functionality per unit of volume. 







# Ultra-High-Speed Analog-to-Digital Conversion Technology

**Mark E. Lowry**

*Physics and Space Technology*

**Ronald E. Haigh**

*Defense Sciences Engineering Division  
Electronics Engineering*

**Charles F. McConaghy**

*Electronics Engineering Technologies Division  
Electronics Engineering*

We have evaluated competing photonic approaches to the problem of high-speed analog-to-digital conversion (ADC). Our study of the existing literature has led to a novel technology that will enable extremely high-fidelity ADCs for a variety of national security missions. High-speed ( $>10$  Gigasamples/s), high-precision ( $>10$  bits) ADC technology requires extremely short aperture times ( $\sim 1$  ps) with very low jitter requirements ( $<10$  fs). These fundamental requirements, along with other technological barriers, are difficult to realize with electronics.

We have conceived a multi-wavelength approach that uses a novel optoelectronic soliton. Our approach uses an optoelectronic feedback scheme with high optical  $Q$  to produce an optical pulse train with ultra-low jitter ( $<5$  fs) and high amplitude stability ( $<10^{-10}$ ). This approach requires low power and can be integrated into an optoelectronic integrated circuit to minimize the size.

## Introduction

Many national security missions, particularly those that are intelligence community-related, involve the application of advanced communication, instrumentation, radar, sensor, and electronic warfare systems. These all rely on ADCs to digitize a large information bandwidth (GHz) with high dynamic range and precision. However, the performance of state-of-the-art ADCs has progressed rather slowly—about 1-bit improvement, or doubling in sampling speed every six to eight years. This can, to a large extent, be attributed to the limitations of the available semiconductor technologies in terms of device matching, device operating frequencies, and noise and nonlinearity in active devices.

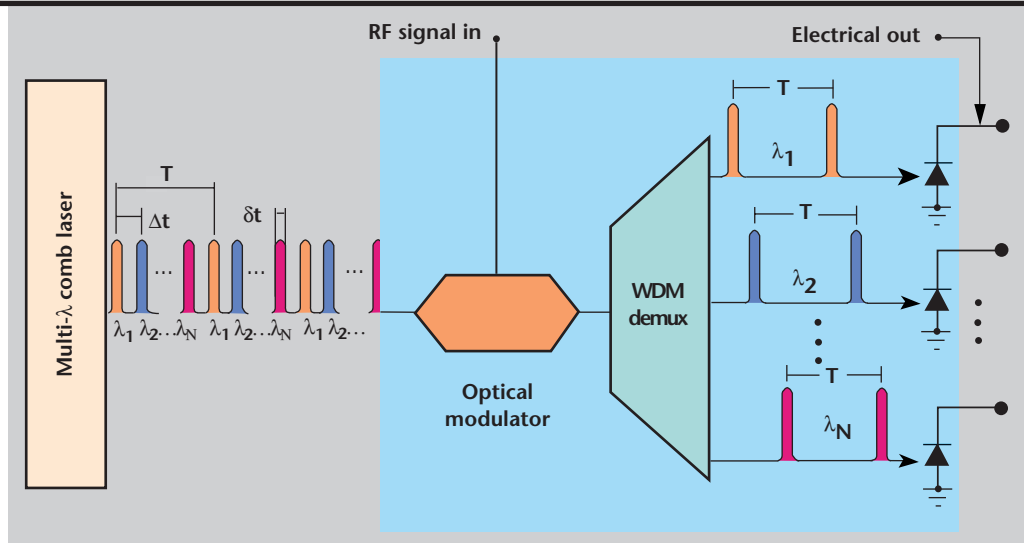
To obtain a quantum leap in performance beyond that of current electronic ADCs, we propose to develop the enabling technology for a class of photonic ADC architectures based on advanced optoelectronic technology. With the unique ultra-high frequency capability of advanced optoelectronic

components, the proposed class of photonic ADCs will simultaneously attain high sampling rates and large dynamic ranges. These photonic ADCs, along with advanced sensor technology, will allow measurement of physical phenomena of nearly every type with unmatched speed and accuracy. For applications that require high precision, but not necessarily fast sample rates, photonic ADCs will enable oversampling at unmatched sample rates to enable ultra-high precision sigma-delta ADC architectures which trade-off sample rate for precision.

## Progress

Our conceived ADC photonic architecture (**Fig. 1**) uses a multi-wavelength ultra-short laser pulse train and a Mach-Zehnder modulator to sample a broadband signal of interest (**Fig. 1**, RF signal in). The sampled signal is temporally demultiplexed through a wavelength division multiplexer to an array of photodetectors where the outputs can then be digitized by a time interleaved array of slower-speed

**Figure 1. Optical Sampler/demultiplexer photonic front-end building block.**



electronic ADCs. We have also envisaged more complex photonic ADC architectures. All require the proposed optical source to sample a signal of interest.

The multi-wavelength comb laser is realized with a novel externally modulated coupled-cavity Fabry-Perot interferometer with optoelectronic feedback (**Fig. 2**). Here the RF input driving the phase modulator will periodically sweep the optical pass-band through the cw wavelengths, simultaneously pulse modulating each wavelength and providing the appropriate temporal spacing for each wavelength in the resulting comb.

A portion of the optical output signal is routed through a fiber delay line back to the phase modulator input, thus, creating a high Q optical feedback circuit. The signal is then bandpass-filtered optically to select only one wavelength of the multi-spectral pulses for detection. The detected signal is bandpass-filtered electrically to eliminate harmonics, and amplified with a low-noise narrowband RF amplifier prior to driving the phase modulator.

The laser source will generate an optical pulse train with pulse widths between 1 and 10 ps and a jitter of 1 to 10 fs. We expect to realize a low-jitter optical pulse train with less than 5 fs of jitter over at least a 1-ms integration window using this approach. This jitter specification is at least an order magnitude improvement over state-of-the-art mode-locked feedback loop semiconductor and fiber lasers. These lasers have relatively large pulse jitter because of the amplified spontaneous emission (ASE) noise present in the lasers.

Because we modulate external to the gain medium, and in the absence of ASE, the timing jitter of our source will be governed exclusively by the effective Q of the optoelectronic circuit and the noise

of the RF amplifier driving the external phase modulator. The long term stability will be governed by the mechanical and temperature stability of the electro-optic Fabry-Perot cavity and the fiber feedback loop.

The multi-wavelength nature of the optical pulse train is required to temporally demultiplex the optically sampled signal. The Fabry-Perot cavity can be simultaneously seeded with lasers of different wavelengths resulting in a multi-wavelength pulse train. Our approach synthesizes the generation of the required ultra-short pulses from an array of continuous wave lasers. Optical pulses with pulsewidths as short as 660 fs have been demonstrated using electro-optic synthesis.

## Recent Accomplishments

Our accomplishments in FY-98 included the following:

1. Several classes of photonic ADC architectures have been conceived. These architectures have many common features including the notion of sampling a signal with a multi-wavelength optical pulse train to allow the signal to be demultiplexed spectrally.
2. A novel multi-wavelength optoelectronic sampling source has been envisioned. The source develops ultra-short optical pulses using external phase modulation in a Fabry-Perot cavity. This approach enables optical pulse trains to be generated with ultra-low jitter characteristics along with high amplitude stability.
3. A mid-year proposal was funded, based on these ideas. Some experimental results have been obtained.

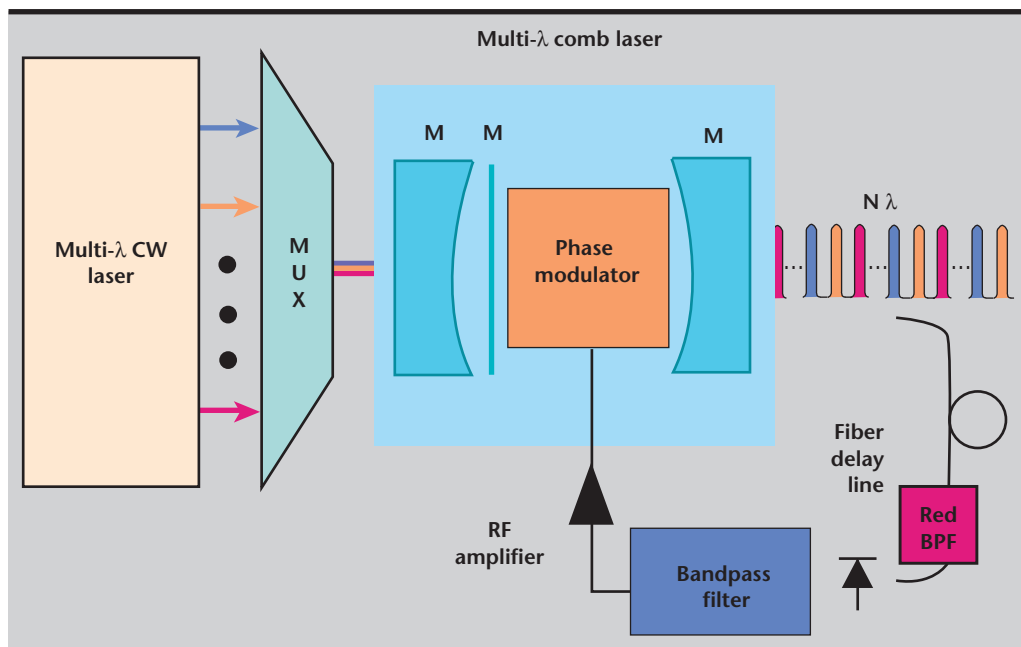



Figure 2. Coupled cavity multi-wavelength comb source with high-Q optoelectronic feedback.

4. A proposal to continue the development of this work with an external sponsor has been developed.

Finally, other applications for the proposed source have been considered, including 1) synthesis of optical sidebands with precise frequency separation for optical spectroscopy; and 2) wavelength encoding schemes for ultra-high (100 fs) temporal resolution of transient events.

## Future Work

It is anticipated that this effort has a high probability of securing funding in FY-99 and is synergistic with other high-speed instrumentation projects at Lawrence Livermore National Laboratory including FemtoScope, RadSensor, and Photonic Doppler Velocimetry. 



# H High-Voltage Photovoltaics

**Karla G. Hagans and Ronald E. Haigh**

*Defense Sciences Engineering Division*

*Electronics Engineering*

This technology-base project is a continuation of research to develop photovoltaic technology to generate voltages up to several kilovolts for powering electrically isolated systems with a fiber optic laser source.

## Progress

This year, we undertook a development effort to successfully demonstrate kilovolt potentials in an electrically isolated manner using photovoltaics and a fiber optic laser source.

In FY-97, our research and development led us to investigate approaches to reducing the photons absorbed in the semi-insulating substrate between adjacent cells. These photons induce photoconductive current between the devices, which tends to shunt the cells. By depositing an absorptive or reflective material on the semi-insulating substrate regions of the device, we could successfully shield the substrate from photons and eliminate the photoconductive current in the substrate.

We designed prototype photovoltaic linear arrays, including the epitaxial structure of the devices, tested the functional, monolithically-integrated 90-V photocells, and evaluated techniques to stack these photocells to generate multiple kilovolts of potential in a compact area. We successfully demonstrated a 1260-V photocell by dicing the individual 90-V photocells and wirebonding fourteen of them in series on a glass substrate.

The photocell is shown in **Fig. 1**.



*Figure 1. Photocell. We demonstrated 1260 V from this photovoltaic device.*





# attice Boltzmann Simulation of Complex Fluid Flows

**David S. Clague**

*New Technologies Engineering Division  
Mechanical Engineering*

This report describes the lattice Boltzmann (LB) method for simulation of complex fluids. LB simulation results for a few flow configurations are considered; namely, results for flow between infinite parallel plates, the Hele-Shaw cell, and flow through a 3-D, ordered array of cylinders. The ability of the LB method to correctly predict the fluid velocity profile in the Hele-Shaw cell is examined, and the error as a function of lattice site density is discussed. The hydraulic permeability, which is a function of the hydrodynamic force acting on a stationary object due to fluid flow, for a 3-D, ordered configuration of cylinders is compared with the results of Higdon and Ford.

## Introduction

Fluid flow has been a topic of engineering importance and research for many years. Traditional methods to solve such problems include exact theory, finite element methods, finite difference methods, finite volume methods and singularity methods. All of these approaches have their roots in the continuum approximation of fluid mechanics or the Navier-Stokes equations. When applied appropriately, these approaches provide a qualitative and quantitative description of flow systems. A relatively recent approach, the LB method, has been growing in utility and popularity in the fluids community.

The LB method has its roots in the kinetic theory of gases<sup>1</sup> or the Boltzmann transport equation. In the limit of small Mach number and small Knudsen number, the Boltzmann transport equation recovers the Navier-Stokes equations of motion. Because the Boltzmann transport equation describes the statistical average motion of fluid molecules, this is not surprising. In contrast, the continuum approaches cited above are macroscopic descriptions that assume that the properties of interest, for example, density, and fluid velocity, are continuous throughout space.

The LB equation can be thought of as the discrete form of the Boltzmann transport equation. Like the Boltzmann transport equation, the LB equation also recovers the Navier-Stokes equations of motion in the limit of small Mach and Knudsen numbers. The LB method provides great flexibility in the study of bounded, particulate media, or complex fluids.

Essentially, the study of complex systems using this approach is limited by the users' ability to describe the medium. For example, a core sample of sand stone was imaged and mapped onto a lattice, permitting the study of two-phase, oil/water, flow through the semi-permeable medium.<sup>2</sup> Additionally, the LB method has only recently found a niche in the engineering community, and therefore is still a novel approach to such problems.

For a detailed description of the theoretical considerations and breadth of application, the reader is encouraged to see the work of Chen and Doolen.<sup>2</sup>

## Progress

Selected results from a recent article<sup>3</sup> and current research efforts are presented in this report to demonstrate the utility of the LB method. Specifically, results for the velocity profile in a Hele-Shaw cell are presented, and the hydraulic permeability calculations for the BCC lattice of cylinders as described by Higdon and Ford<sup>4</sup> using the LB method are compared with their Spectral Boundary Element results for the same system. In the conclusions a brief description of future work at Lawrence Livermore National Laboratory (LLNL) is discussed.

## The Hele-Shaw Cell

Many flow systems of interest involve bounded flows. A well-known example of such a system is the Hele-Shaw flow cell. The Hele-Shaw cell was put

forth as a representation of a porous medium, as shown in **Fig. 1**.

The flow cell is periodic in both the  $x_1$  and  $x_2$  directions; hence, the unit cell gets replicated throughout space in the  $x_1$ - $x_2$  plane. The imposed flow is in the  $x_1$  direction. Essentially, the vertical gap,  $H$ , between bounding walls represents the equivalent, average distance between fixed obstacles in a porous medium.

LB simulations were performed to study pressure-driven flow in this configuration and compared with the analytic solution. In lattice space, a pressure gradient is imposed by applying a constant body force on the fluid lattice sites between the walls. A representative fluid velocity profile is compared with exact theory in **Fig. 2**. The error between the LB result and the analytic solution is approximately 0.5%, on average.

Similar simulations were run for various node densities across the gap,  $H$ , and the spatial convergence is approximately second order.

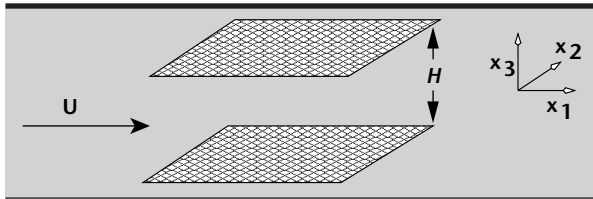


**Figure 1.** Hele-Shaw cell. The flow direction is in the  $x_1$  direction, and the simulation cell is periodic in both the  $x_1$  and  $x_2$  directions.  $H$  is the vertical distance between the solid, infinite parallel planes.

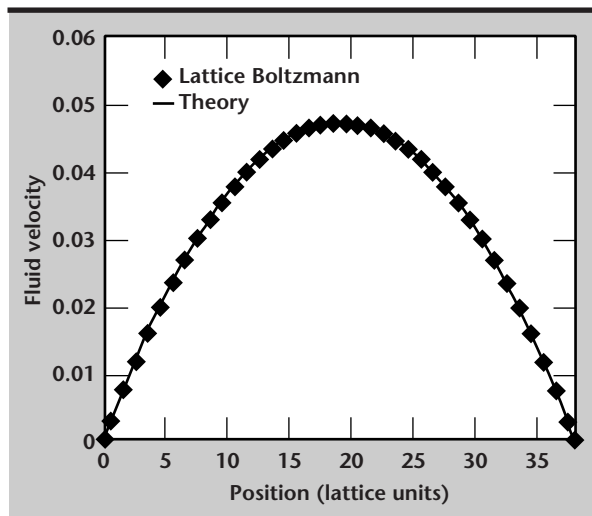


**Figure 2.** Fluid velocity profile. The LB result is compared with exact theory for pressure-driven flow in a Hele-Shaw cell. The separation,  $H$ , in lattice space is 38 lattice sites.

### Three-Dimensional BCC Lattice of Cylinders

Flow through fibrous media is common in many filtration systems. Examples range from man-made air filters to blood filtration in the kidney; hence, the ability to predict flow behavior in such systems is of paramount importance. The BCC lattice<sup>4</sup> provides a rigorous test of the LB method for flow through 3-D fibrous media. An LB representation of a typical BCC simulation cell is shown in **Fig. 3**.

The solid lattice sites represent the solid phase, and the clear or unmarked lattice sites represent the fluid phase. For visual clarity, the cylinder radius is only three lattice sites, but for the actual simulation results, the cylinder radius was increased to increase the force resolution at higher fiber volume fractions,  $\phi$ . Flow is imposed here, again, by applying a uniform body force on the fluid lattice sites. To enforce the no-slip condition in the LB method, the fluid is “bounced back” to originating lattice sites that are adjacent to the solid surfaces.<sup>2,3</sup> Therefore, knowing the pressure gradient,  $\nabla P$ , the superficial average fluid velocity,  $\langle \underline{u} \rangle$  and the fluid viscosity,  $\mu$ , one can make use of Darcy’s law,

$$\langle \underline{u} \rangle = -\frac{k}{\mu} \nabla P, \quad (1)$$

and calculate the hydraulic permeability,  $k$ , of the medium.

In the results shown in **Fig. 4**, the actual cylinder radii ranged from 5 to 30 lattice sites or lattice units.

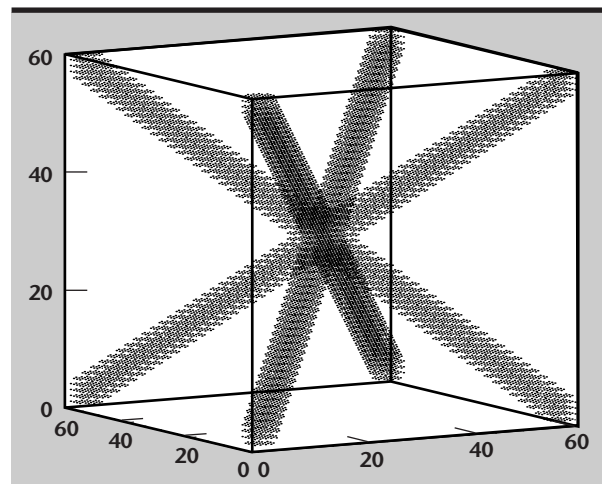


**Figure 3.** Three-dimensional, BCC lattice. The cylinders depicted have a radius of three lattice units. Cylinders emanate from the center of the cell and intersect the eight vertices of the cubic domain. The dimensions of the simulation cell are  $60 \times 60 \times 60$ , which represents a fiber volume fraction that is approximately equal to 0.36.

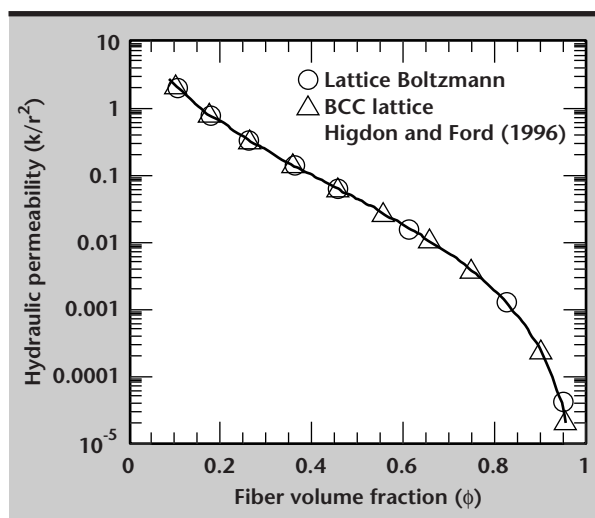



Figure 4. Hydraulic permeability for the BCC lattice of cylinders. LB results are compared directly with Spectral Boundary Integral results.

As shown, the hydraulic permeability, made dimensionless with the cylinder radius,  $r^2$  is plotted as a function of fiber volume fraction,  $\phi$ . Here LB simulation results are compared with the result from the Spectral Boundary Element Methods of Higdon and Ford<sup>4</sup> for the BCC lattice configuration. Their approach is both rigorous and accurate for nearly all possible fiber volume fractions. As is clearly seen here, the LB results are nearly identical to that of Higdon and Ford<sup>4</sup> over the entire range of fiber volume fractions considered. This is remarkable since many methods fail when considering fiber volume fractions  $>0.5$ .

## Future Work

The LB method is indeed a powerful tool for the study of fluid flow through complex media. The simulation results above confirm that it is as accurate as the best methods available, Spectral Boundary Integral Methods, for solving Stokes flow problems. The LB results represent building blocks for modeling and simulation of systems of greater complexity. Our research focuses on using LB methods to study transport phenomena issues relevant to current and future efforts in LLNL's Microtechnology Center.

## References

1. Landau, L., and E. M. Lifshitz (1989), "A Course of Theoretical Physics, Volume 10," Pergamon Press.
2. Chen, S., and G. D. Doolen (1998), "Lattice Boltzmann method for fluid flows," *Ann. Rev. Fluid Mech.*, **30**, pp. 329-364.
3. Clague, D. S., B. D. Kandhai, R. Zhang, and P. M. A. Soot (1998), "The hydraulic permeability of (un) bounded fibrous media," submitted to *J. Fluid Mech.*
4. Higdon, J. J. L., and G. D. Ford (1996) "Permeability of three-dimensional models of fibrous porous media," *J. Fluid Mech.*, **308**, p. 341. 



# **M**icro-Electromechanical Systems (MEMS) for Characterization of Plastic-Bonded Explosives

**Jeffrey D. Morse**

*Electronics Engineering Technologies Division  
Electronics Engineering*

**Dino R. Ciarlo**

*Engineering Research Division  
Electronics Engineering*

**Scott E. Groves and Diane J. Chinn**

*Manufacturing and Materials Engineering Division  
Mechanical Engineering*

**Mehdi Balooch**

*Defense and Nuclear Technologies*

**Mark J. LaChappel**

*Defense Sciences Engineering Division  
Electronics Engineering*

Nano-indentation using custom microprobes within an atomic force microscope (AFM) can be an extremely valuable tool for characterization of mechanical and viscoelastic properties of materials at the microscale level. We have used AFM nano-indentation to characterize the mechanical properties of mock plastic-bonded explosives (PBX). Characterization of the materials properties at the microscopic level enables better understanding of the aging mechanisms of these materials. Micromachining techniques have also been used to design calibrated experiments to assist in interpreting the nano-indentation results under various circumstances.

## **Introduction**

One of the key problems in support of stockpile stewardship is the characterization of aging mechanisms for polymer binder materials used in PBX in various shapes and housings. Understanding the mechanical properties of PBX materials systems under accelerated aging conditions can provide valuable insight into the failure mechanisms of these materials, and subsequently, the lifetime of stockpile systems and devices.

Typical high-explosive (HE) crystallites in binder materials have dimensions on the order of 10 to 50  $\mu\text{m}$ , with distances between crystallites as small as 5  $\mu\text{m}$ . While mechanical properties of the binder material characterized at the macro-scale are important, it is critical to understand the micro-scale

properties of the binder material, as well as the HE/binder interface.

Micromachined structures and devices provide characterization tools with these properties over  $\mu\text{m}$  scale dimensions. At present, micromachining technologies have focused on the fabrication of custom micro-probes for AFM nano-indentation measurements and custom templates to form reservoirs of binder materials for calibrated nano-indentation experiments. Nano-indentation enables the time-dependent mechanical properties of the binder material to be measured. With a fixed load applied to the AFM-nano-indenter, the micro-scale equivalent of a creep test is performed by monitoring how the nano-indenter plastically displaces with time. In this manner, the viscoelastic properties of the binder material can be characterized.



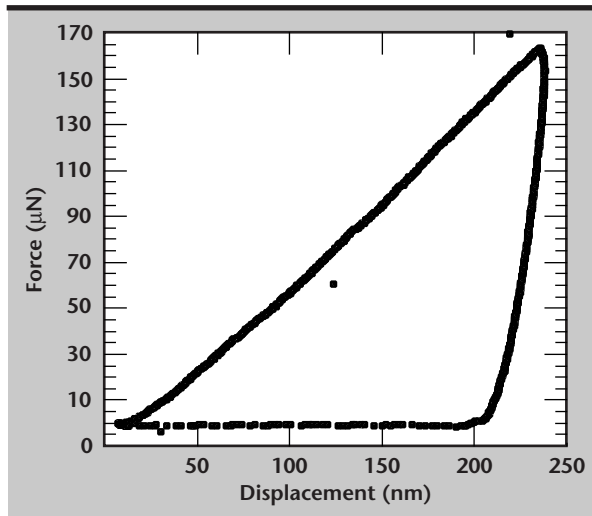


Figure 1. Force vs time information.

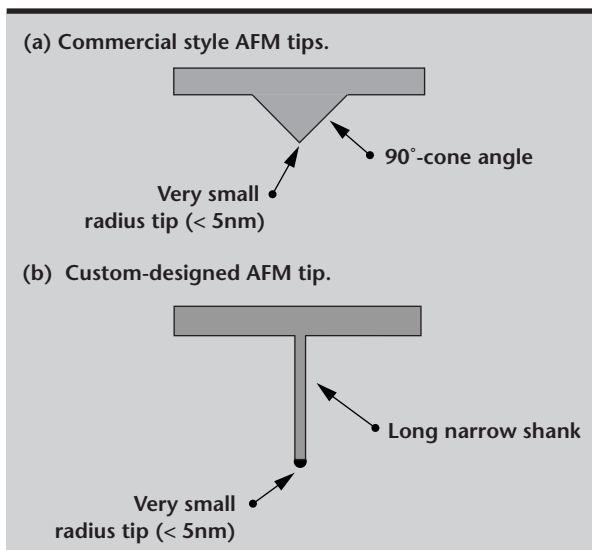


Figure 2. Sample nano-probe showing that (a) existing AFM tips cannot be used to probe surfaces with deep and narrow crevasses, and (b) tall thin probes can reach deep into crevasses.

## Progress

Nano-indentation measurements were performed on mock PBX using an AFM system at Lawrence Livermore National Laboratory (LLNL). The AFM is modified with a transducer-indenter assembly called a Micromechanical Testing Instrument. Like its conventional counterpart, the instrument can image the topography of specimens by tracing the superficial contours of the sample with a constant sub- $\mu\text{N}$  load.

In addition, the device is a force-generating and depth-sensing instrument capable of generating load-displacement curves at specified locations. The local mechanical properties such as stiffness,

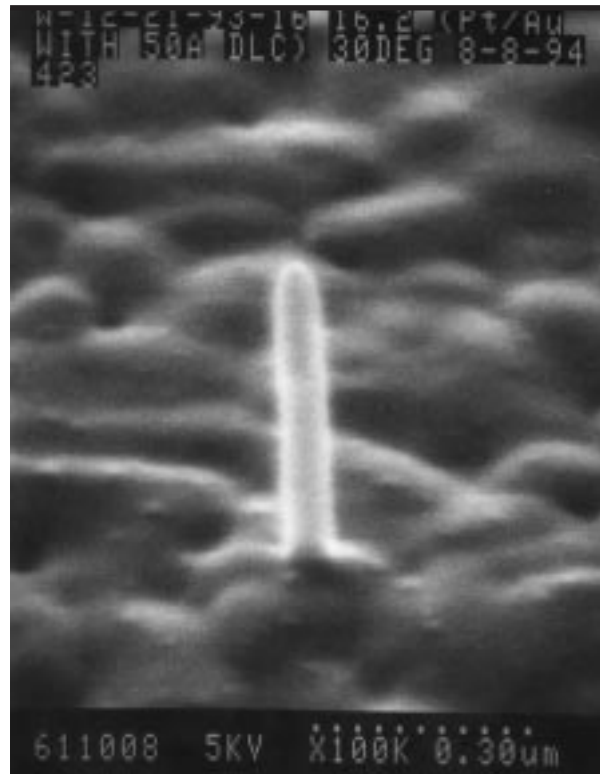


Figure 3. Structure formed by electroplating through a template patterned in a resist film.

hardness, and elastic modulus can be determined. The stiffness is defined as the slope of the force/displacement curve during unloading. The elastic modulus,  $E$ , and hardness,  $H$ , are defined as:

$$E = \pi^{1/2} / (2a^{1/2}) S \quad \text{and} \quad H = F_{\max} / a$$

where  $S$  is the contact stiffness,  $F_{\max}$  is the maximum load and  $a$  is the projected contact area under the load. The resulting force vs time information is illustrated in **Fig. 1**.

While these results provide important information regarding the mechanical properties of moderately homogeneous binder material, the problem becomes much more complex with the addition of HE crystallites. For this case, custom microprobes of predetermined size and shapes must be used, typically with tip shank diameters  $< 0.5 \mu\text{m}$  and aspect ratios  $> 10:1$ . These can be designed and fabricated by micromachining techniques and mounted on the AFM fixture.

It would be desirable to be able to characterize the mechanical properties of the HE/binder interface, as well as regions between crystallites as narrow as  $5 \mu\text{m}$ . This desire arises due to concerns that the interface becomes fatigued by aging, leading to delamination and eventual failure of the material.

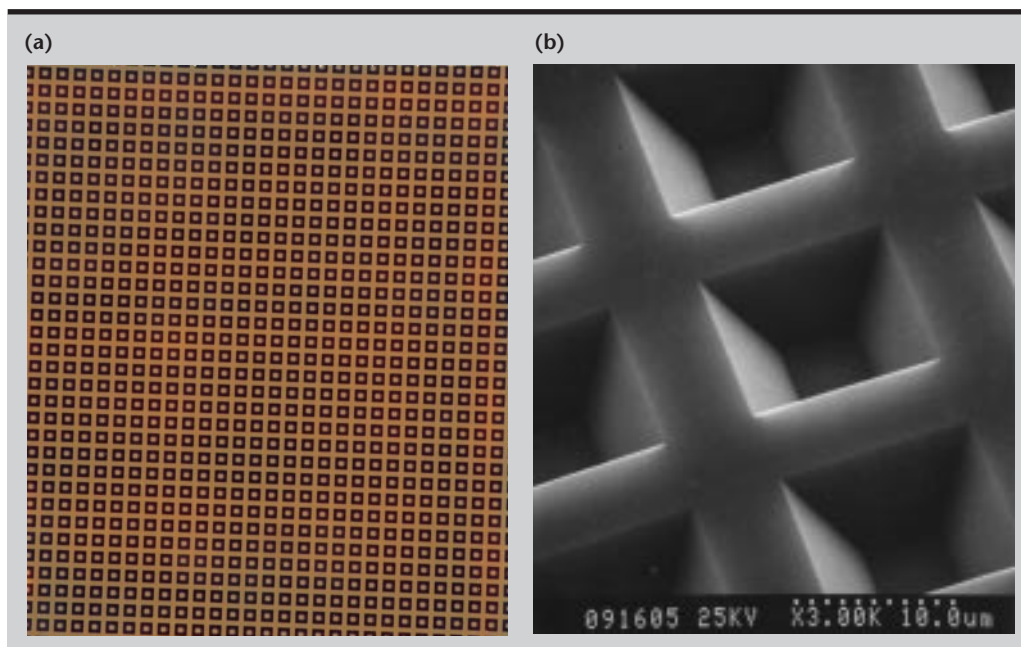


*Figure 4. Custom template micro-machined in silicon substrate for calibration studies of nano-indentation techniques on mock PBX: (a) photograph; (b) SEM image.*

To accurately characterize the mechanical properties of the interface and narrow regions, the AFM nano-indenter probe can be scanned across the HE/binder interface. Using this technique, a smaller diameter ( $<0.5\ \mu\text{m}$ ) probe is required which is cylindrical, with an aspect ratio on the order of 10:1. Thus, the probe exerts force on a constant surface area which can access extremely narrow areas.


An example of the required nano-probe is illustrated in **Fig. 2**, which compares this requirement to relatively standard AFM probes. A variety of micro-fabrication techniques can be used to realize this small-diameter, high-aspect-ratio structure.

**Figure 3** shows a  $1\text{-}\mu\text{m}$ -high,  $0.1\text{-}\mu\text{m}$ -diameter structure formed by electroplating through a template patterned in a resist film. Similar structures can be formed through precision plasma etching techniques and are presently under development in a structure which can be retrofit onto the AFM system.

Finally, a custom template to form reservoirs was fabricated using photolithography to define patterns in a silicon nitride mask on a silicon substrate with

areas ranging from 5 to  $25\ \mu\text{m}$  on a side. Wells were then etched in the silicon with various depths ranging from 5 to  $25\ \mu\text{m}$ . This is shown in **Fig. 4**. The wells are then filled with binder material, and AFM nano-indentation measurements are performed as means to calibrate the resulting mechanical response of the binder in proximity to the interface and as a function of depth to a hard surface beneath the probe region. This will provide important information regarding the three-dimensional nature of the samples being characterized.

## Future Work

Custom reservoir templates have been fabricated in silicon and are presently being prepared for deposition of mock PBX. AFM nano-indentation measurements will be performed to provide a comparison between standard AFM probes and custom AFM probes, as described above. The custom AFM probes must be fabricated in a structure which is readily mounted in the AFM system for calibration and measurements. 



# **M**icro-Electromechanical-Systems-(MEMS)-Based Fuel Cell Technology

**Jeffrey D. Morse and Robert T. Graff**

*Electronics Engineering Technologies Division  
Electronics Engineering*

**Alan F. Jankowski and Jeffrey P. Hayes**

*Materials Science and Technology Division  
Chemistry and Materials Science*

We have fabricated a fuel cell stack which uses thin-film electrodes, catalysts, and ion-conducting layers deposited by physical vapor deposition techniques. The stack has been patterned with electrical connections using standard micro-fabrication techniques, and subsequently formed into free-standing membranes by micro-machining away the silicon substrate. Manifold structures have also been fabricated through silicon micro-machining techniques.

## **Introduction**

A serious need exists for portable power sources with significantly higher power density, longer operating lifetime, and lower cost. Present rechargeable and primary portable power sources have excessive weight, size and cost, with limited mission duration. As an example, batteries covering a power range from 1 to 200 W have specific energies, ranging from 50 to 250 Wh/kg, which represents 2 to 3 h of operation for a variety of commercial and military applications.

An alternative power source is the fuel cell, which potentially provides higher performance power sources for portable power applications if the stack structure, packaging, and cell operation are made compatible with scaling down of size and weight.

Fuel cells typically consist of electrolyte materials, either polymer or solid oxide, which are sandwiched between electrodes. The fuel cell operates by delivering fuel (usually hydrogen) to one electrode, and oxygen to the other. By heating the electrode-electrolyte structure, the fuel and oxidant diffuse to the electrode interfaces, where an electrochemical reaction occurs, releasing free electrons and ions which conduct across the electrolyte.

Typical fuel cells are made from bulk electrode-electrolyte materials which are stacked and manifolded using stainless steel packaging. These systems are bulky and operate at high temperatures (>600 °C). If the electrode-electrolyte stack can be

made very thin and deposited using thin-film deposition techniques, the temperature of operation will be significantly lower.

Previous efforts at Lawrence Livermore National Laboratory (LLNL) have demonstrated the synthesis of a thin-film solid-oxide-based electrolyte fuel cell (TFSOFC) stack.<sup>1,2</sup> The TFSOFC stack was formed using physical vapor deposition (PVD) techniques. The host substrate was a silicon wafer covered by a thin layer of silicon nitride. A layer of nickel was first deposited, followed by a layer of yttria-stabilized zirconia (YSZ).

The conditions during the deposition were adjusted to achieve smooth, dense, continuous films, thus avoiding pinhole formation which could result in electrical shorting through the electrolyte layer. This enables the electrolyte layer to be on the order of 1  $\mu\text{m}$  thick, rather than typical thicknesses on the order of >10  $\mu\text{m}$  for bulk solid-oxide fuel cells.

By thinning the electrolyte layer, resistive losses are significantly lower, and the fuel cell operates at much lower temperatures. A silver electrode layer is deposited on top of the YSZ layer. The deposition conditions of this film are adjusted to create a porous structure so that oxygen can readily diffuse to the electrolyte interface.

## **Progress**

During the past year, this effort has focused on the utility of a TFSOFC, along with assessments for

other electrolyte materials systems. The incorporation of manifold structures within the host substrate through micro-machining techniques enables a complete fuel cell device to be realized which can be readily attached to fuel and oxidant sources. This concept is illustrated in **Fig. 1**.

In this approach, the fuel cell stack is created by thin-film deposition techniques. Integrated-circuit type micro-fabrication processes are used to pattern electrode contacts, as well as to form a resistive heater element within the stack structure.

The stack is subsequently formed into a free-standing membrane by selective etching of the substrate. Manifold channels are micro-machined in another substrate, which is subsequently bonded to the fuel cell substrate, as illustrated in **Fig. 1**.

This approach provides an effective means to form efficient fuel cell stack and electrode structures monolithically, and distribute fuel to the entire stack without the need for bulky complex manifolding. Furthermore, since the stack is now only a small percentage of the mass of the entire structure,

appropriate thermal design of the fuel cell device, package, and resistive heating elements will allow efficient, low-power heating of the stack.

**Figure 2a** illustrates a completely fabricated fuel cell module with integrated heating element, with a view of the fuel cell stack free-standing membranes shown in **Fig. 2b**. To achieve this, the silicon substrate was selectively etched with potassium hydroxide, using patterned silicon nitride as the mask.

Manifold channels, shown in **Fig. 3**, were etched in a silicon substrate using similar techniques. These components will ultimately be bonded together to form a fuel cell module having inlet and outlet channels with approximately  $50\text{-}\mu\text{m} \times 200\text{-}\mu\text{m}$  openings for fuel delivery.

The MEMS-based thin-film fuel cells are tested to measure the current output as a function of temperature as the voltage is incremented from nil through and above the open circuit voltage (OCV). The solid-oxide fuel-cell (SOFC)-layered combination of a Ni-YSZ anode, YSZ electrolyte, and Ag-YSZ cathode, allows

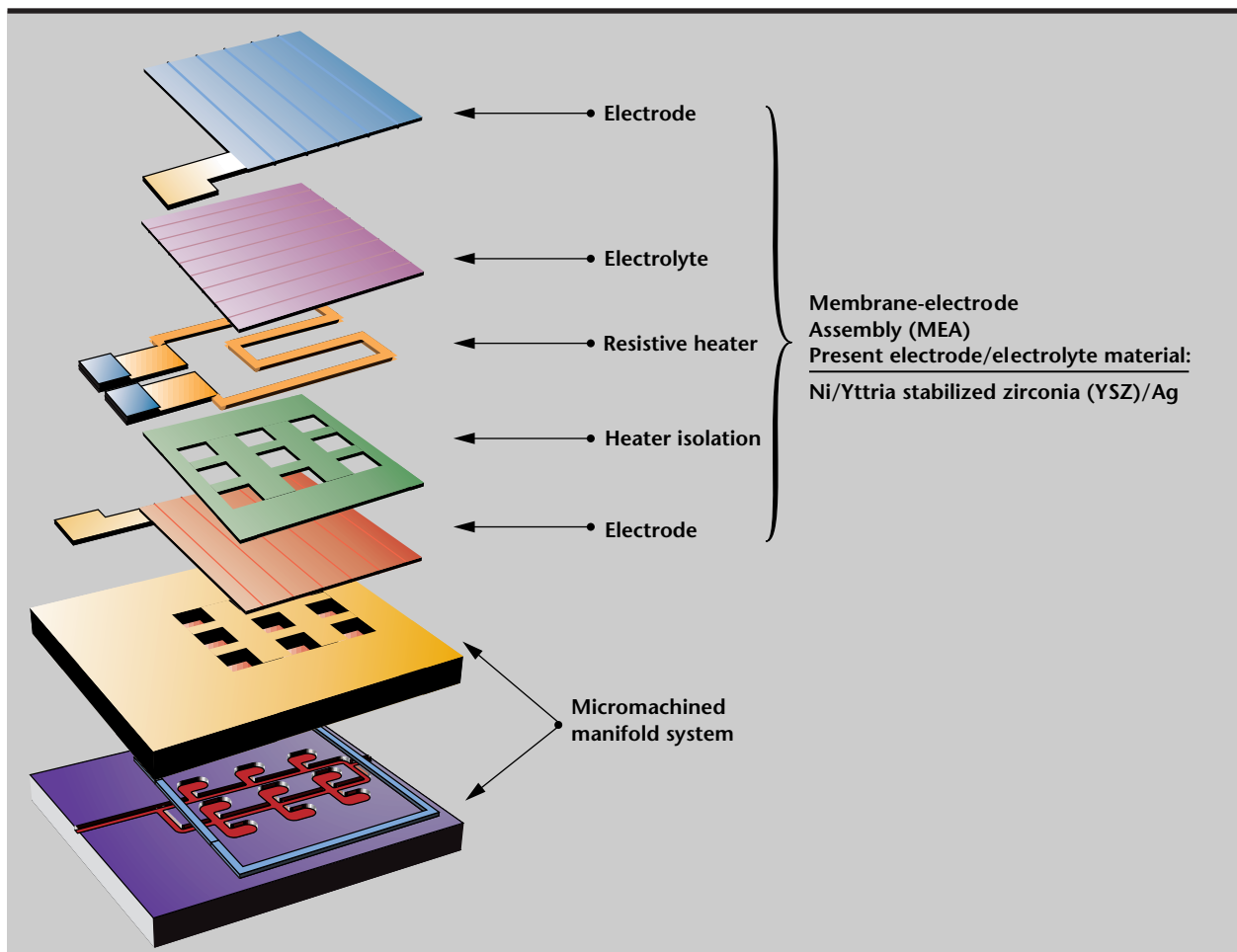


**Figure 1.** MEMS-based fuel cell concept using silicon micro-machined host structure and manifold system with fuel cell stack membranes.

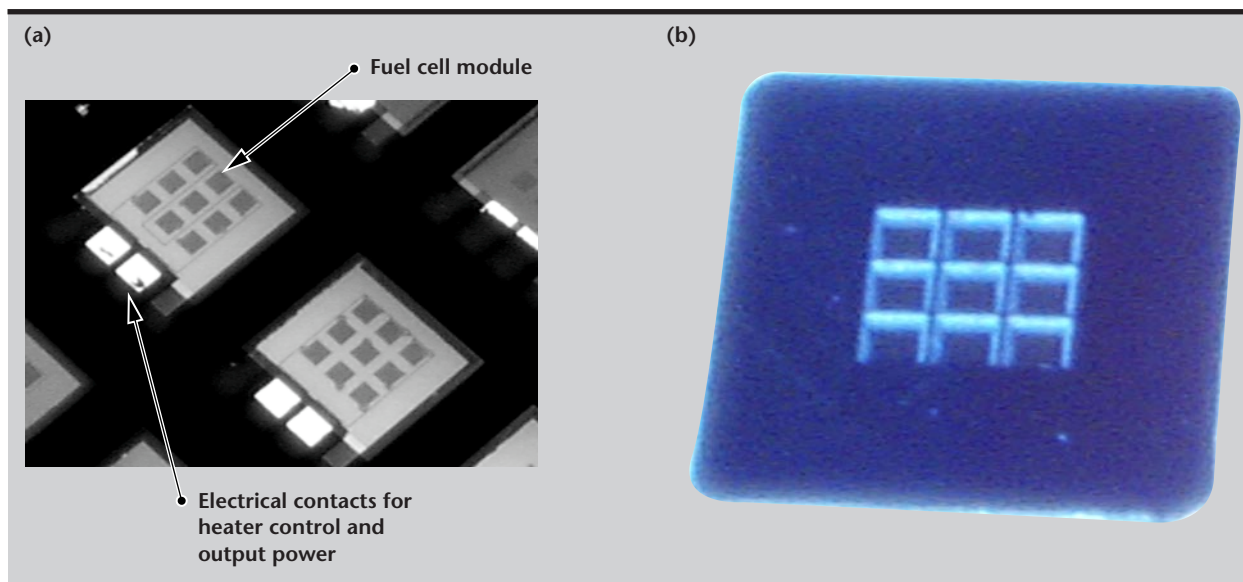


Figure 2. (a) Micro-fabricated fuel cell module, with (b) free-standing thin-film fuel cell stack membrane, formed by micro-machining silicon from backside.



Figure 3. Fuel cell module with micro-machined manifold channels in bottom wafer.

for the transport of oxygen ions through the electrolyte via a diffusion-moderated process. The resistivity of the electrolyte is measured to typically exceed  $1 \text{ M}\Omega\text{-cm}$ .

Once an oxygen ion diffuses through the electrolyte and combines with hydrogen, an (electron) current is generated. A maximum OCV of  $\sim 1.1 \text{ V}$  exits for the combination of oxygen and hydrogen using this SOFC structure.

The TFSOFC sits atop a windowed silicon wafer that is bounded on the anode side to a quartz tube using a ceramic epoxy. The anode and cathode tabs on the silicon wafer are silver-epoxy bonded to silver wires. The wires are connected to a semiconductor parameter analyzer that controls the applied

cell potential. The silicon-wafer-mounted tube is O-ring-sealed within a larger diameter quartz tube that is placed within a conventional (Lindbergh) clam-shell furnace.

Feedthroughs are provided at either end of the assembly, on both the anode and cathode sides, that allow the passage of the oxidant and fuel as gases. A fuel mixture of 3% hydrogen is flowed through the anode tube at a rate of 1 to 3 sccm. Air is flowed to the cathode surface at a rate of 1 to 3 sccm. The current-voltage output is measured as a function of temperature to  $600^\circ\text{C}$ .

Initial results of this<sup>o</sup> testing are illustrated in **Fig. 4**. While not optimal, these results exhibit the expected overpotential for this electrolyte materials system with no output current, along with increasing current output as temperature increases.

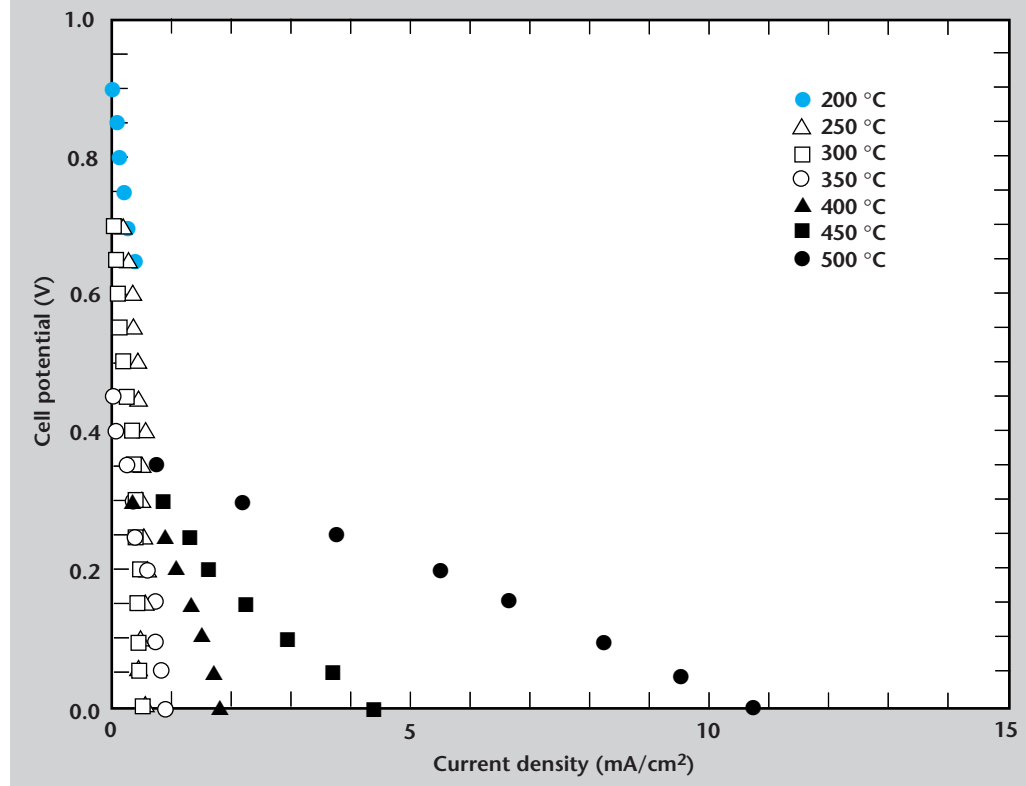
While the output current densities are low, inherent limitations are present in fuel cell performance resulting from the high density of the nickel cathode layer. Thus, while fuel can readily diffuse through the nickel film to the electrolyte interface, water, the byproduct of the electrochemical reaction, is unable to diffuse away from the interface. Thus the reaction ions quench, resulting in limited efficiency of the fuel cell stack.

## Future Work

The next iteration of fuel cell modules will include porous nickel electrode structures, thereby eliminating the effects of water vapor trapped at the electrolyte interface. Further efforts will focus on



Figure 4. Current-voltage characteristics of thin-film solid-oxide fuel cell at various temperatures.



optimizing the design of the heating element and fuel cell stack, and packaging. This includes investigation of alternate electrolyte material, both solid-oxide and solid-polymer systems.

## References

1. Jankowski, A. F., and J. D. Morse (1998), *Materials Research Society Symposium Proceedings* Vol. 496, pp. 155–158.
2. Jankowski, A. F. (1998), U.S. Patent No. 5,753,385, May 19.



# High-Power GaN Microwave Device Technology

## **Glenn A. Meyer**

*New Technologies Engineering Division  
Mechanical Engineering*

## **Gregory A. Cooper and Stacy L. Lehew**

*Electronics Engineering Technologies Division  
Electronics Engineering*

## **Thomas W. Sigmon and Daniel Toet**

*Information Science and Technology Program  
Lasers*

## **Steven DenBaars and Umesh Mishra**

*University of California  
Santa Barbara, California*

The purpose of this work was to develop more efficient doping processes for use in gallium-nitride (GaN)-based power microwave devices. We developed a pulsed laser processing technique aimed at activating n-type dopants for GaN field effect transistors. The laser processing is performed using a XeCl excimer laser with a 35-ns pulse length at a wavelength of 308 nm. This technology allows selective area doping of GaN, presently a major technology roadblock in the fabrication of devices in this material system.

## **Introduction**

GaN is an ideal semiconductor material system for high-power microwave applications due to its unique properties: high thermal conductivity, high temperature stability, high breakdown field strength, and high carrier velocities. Researchers at the University of California, Santa Barbara recently demonstrated<sup>1</sup> GaN-based microwave devices operating at cw power densities greater than 3 W/mm gate width, at a frequency of 18 GHz. This performance is approximately three times higher than the best commercially available devices made from SiC or InP.

High-power microwave amplifiers presently used for communications and radar applications use bulky vacuum tube electron beam devices, such as traveling wave tubes, magnetrons and gyrotrons. Traveling wave tubes, for example, are typically tens of centimeters in size. An all-solid-state, high-power microwave amplifier would enable the development of much smaller and lighter microwave systems for

use in satellite and ground based communications, and remote sensing. Compact devices and antennas enable the construction of phased-array radars with the ability to form steerable beams. Moreover, the DC to RF conversion efficiencies for solid-state transmitters is significantly higher than conventional, high-power RF electron beam devices.

Currently, the performance of GaN-based RF devices is limited by high operating temperatures. This is primarily due to resistive heating in two regions of the device, namely the resistance between the metal contact and the doped semiconductor contact layer (that is, the specific contact resistance) and the total resistance of the doped semiconductor layer. By increasing the number of electrical carriers in the semiconductor layer, the resistive heat generation in both of these regions can be reduced. However, one of the main obstacles to the full realization of the potential of GaN as a material for optoelectronic and microwave devices is the difficulty in reaching high enough doping levels in this material for fabricating low sheet resistance layers.

The most common technique used for doping GaN is incorporation of the dopant atoms into the material during crystal growth. Magnesium is the most common dopant used to create p-type material in metal-organic chemical vapor deposition (MOCVD) growth. The ionization energy of the Mg acceptor in GaN is 150 meV. This value is large enough to result in only a fraction of a percent of the Mg atoms being electrically active at room temperature.<sup>2</sup> This low ratio of electrical carriers to dopant atoms forces the growth to include a significantly higher level of Mg to achieve the desired carrier concentrations. Incorporation of high dopant concentrations causes the normally transparent GaN to become cloudy, indicating large concentrations of crystal defects. Presently, the p-type carrier concentrations achievable with magnesium are in the range of  $2$  to  $3 \times 10^{18}$  holes/cm<sup>3</sup>, a value that is not high enough to achieve low sheet resistance layers or electrical contacts.

Ion implantation may offer a practical solution to the problems associated with achieving high p-type carrier concentrations in GaN. This technique is widely used in semiconductor device fabrication technology. Several researchers have investigated this technique for GaN but have encountered problems that do not appear for Si or GaAs. One of these problems is the high temperature required to incorporate the implanted dopant atoms into the crystal lattice. The effective incorporation of the dopants onto the correct crystal sites and removal of the implant damage requires annealing temperatures in excess of 1200 °C. Nitrogen, being a fundamental constituent of GaN, has a very high vapor pressure at the required annealing temperatures (>1000 bar). Therefore, annealing GaN material at these temperatures requires very robust capping layers to prevent the nitrogen from escaping.

Attempts to use rapid thermal annealing (RTA) have also resulted in thermal budgets well in excess of the levels tolerable for device fabrication. In addition, heterojunctions and quantum wells are particularly sensitive to annealing temperatures in excess of 900 °C. The time-temperature product must be limited to prevent serious degradation of the device layers.

A promising technique useful for reducing the time-temperature product is pulse laser annealing. Near-surface heating by absorption of a pulsed laser beam is expected to allow higher processing temperatures. This typically is a very fast, non-equilibrium process. For example, a 90 nm a-Si film on a low-temperature glass substrate can, following the absorption of a short laser pulse, fully melt and

recrystallize within 150 ns, while the glass remains unaltered. A pulsed excimer laser can deposit large amounts of energy into a thin layer at the GaN surface in a very short time. Deeper layers, containing sensitive quantum structures, do not experience the high temperatures.

The objective of our project was to investigate a pulsed laser processing method for improving the doping activation process for n-type dopants in GaN field effect transistors. The laser annealing actually results in the melting of the implanted layer. During the recrystallization of the molten layer, the doping impurity assumes the appropriate lattice position, allowing realization of the desired low sheet resistance contact layer. This process technology has been demonstrated at Lawrence Livermore National Laboratory (LLNL) to provide very low electrical resistance contacts on Si, SiGe, and SiC semiconductor materials.

## Progress

The initial phase of our research focused on the effects of the pulsed laser process on intrinsic GaN. Once the laser material interactions were understood, laser activation of ion implanted n-type and p-type dopants was investigated. The band gap of GaN semiconductor materials is approximately 3.4 eV, making it ideal for strong absorption of our 4 eV XeCl laser ( $\lambda = 308$  nm) pulse. The laser absorption depth in the GaN is approximately 120 nm, using an absorption coefficient of  $8.37 \times 10^4/\text{cm}$  at  $\lambda = 308$  nm.<sup>3</sup>

The GaN films used in the experiments were 2  $\mu\text{m}$  thick, grown in a modified two-flow horizontal reactor on c-plane sapphire, using low-pressure MOCVD. The chemical precursors used were trimethylgallium (TMGa) and ammonia (NH<sub>3</sub>). The samples were then ion-implanted at an energy of 150 keV with Si and Mg to doses of  $8 \times 10^{16}$  cm<sup>-2</sup> and  $5 \times 10^{14}$  cm<sup>-2</sup>, respectively.

Laser processing of GaN films is performed using a XeCl excimer laser (from Lambda Physik, Germany) with a 35-ns pulse length at a wavelength of 308 nm. The transformation induced in the GaN by this pulse is monitored *in situ* and in real time by measuring the time-resolved transmission (TRT) of an IR laser beam passing through the center of the spot irradiated by the XeCl laser. The samples are held in a vacuum cell with a quartz front window that is transparent to the excimer laser beam. Prior to laser processing, the sample chamber is evacuated to  $1 \times 10^{-3}$  Torr, using a Varian sorption pump. The chamber is then backfilled with flowing nitrogen.

**Figure 1** shows the IR TRT profiles measured during the exposure of an undoped film to pulses at different energy fluences. As seen in this figure, the IR transmission drops dramatically upon laser exposure at fluences greater than threshold. This drop is associated with the heating and melting of the film following the absorption of the excimer laser light. The molten material blocks the IR beam due to its metal-like optical properties.

The transmission signals take more than 2  $\mu\text{s}$  to return to their pre-pulse levels for the highest annealing fluence, indicating that the annealed material cools down slowly. This slow cooling rate is attributed to the fact that the thermal gradient across the film is very small, due to the relatively

deep penetration (120 nm) of the 308-nm light in the GaN. Ultimately, we intend to confine the melting to a shallower region near the surface. Moreover, optical inspection of the films reveals that for laser exposures above threshold a roughening of the films resulted.

**Figure 2** shows the results obtained during the exposure of a sample that was first implanted with Mg ions to a dose of  $5 \times 10^{14} \text{ cm}^{-2}$ , and a depth of 100 nm. The most striking feature of this TRT plot is the fact that the melting duration is now much lower than that of the unimplanted sample. This implies that the implantation altered the optical absorption properties of the film, probably due to surface amorphization.

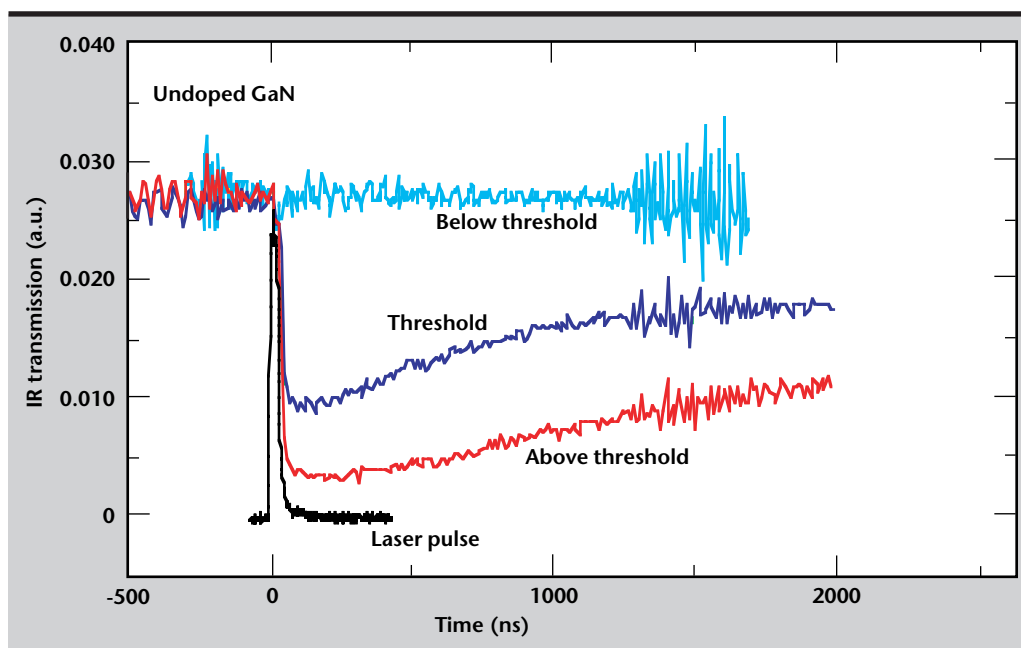


*Figure 1. IR time-resolved transmission profiles obtained during laser exposure of undoped GaN film to various excimer laser fluences. The IR transmission drops dramatically upon laser exposure with threshold fluence indicating that surface melting occurred.*

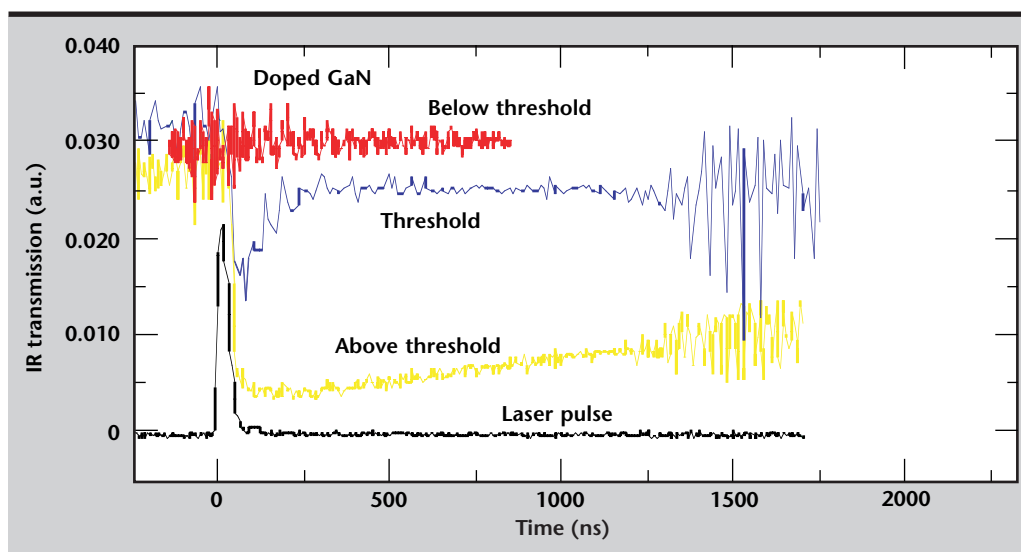


*Figure 2. IR time-resolved transmission profiles resulting from laser exposure of Mg ion-implanted GaN film ( $\text{Mg dose} = 5 \times 10^{14} \text{ cm}^{-2}$ ) to laser pulses with different energy fluences. The IR transmission drops dramatically upon laser exposure with threshold fluence indicating that surface melting occurred.*

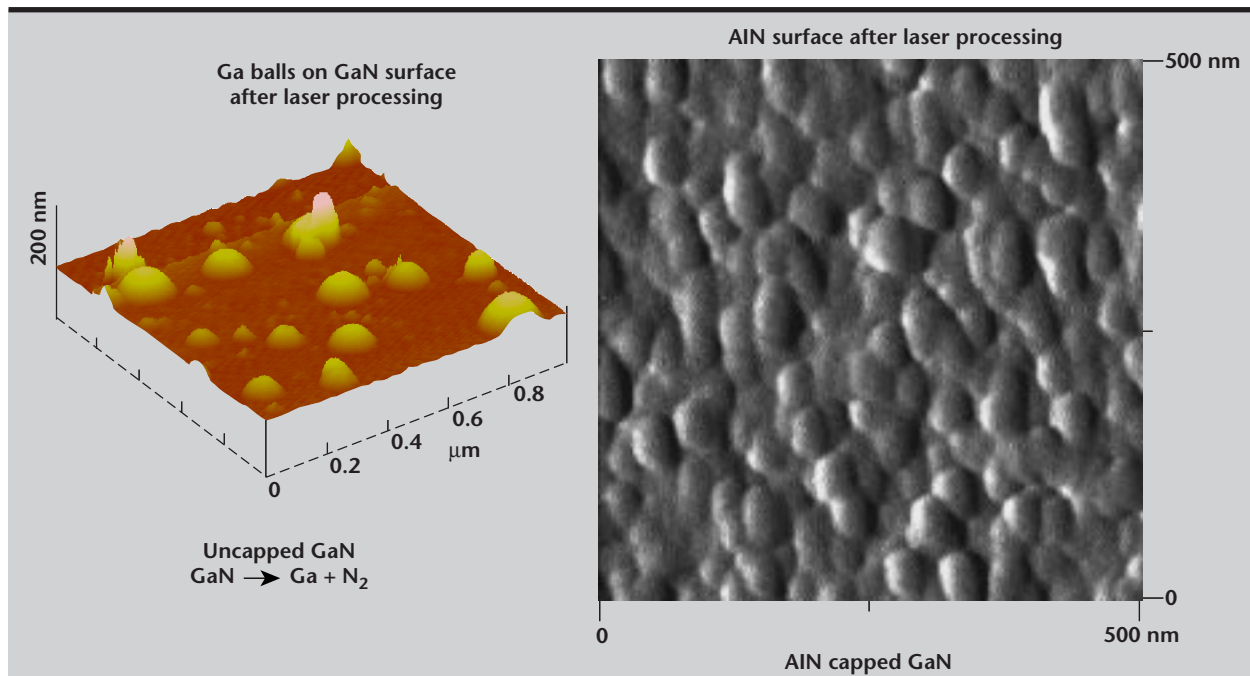
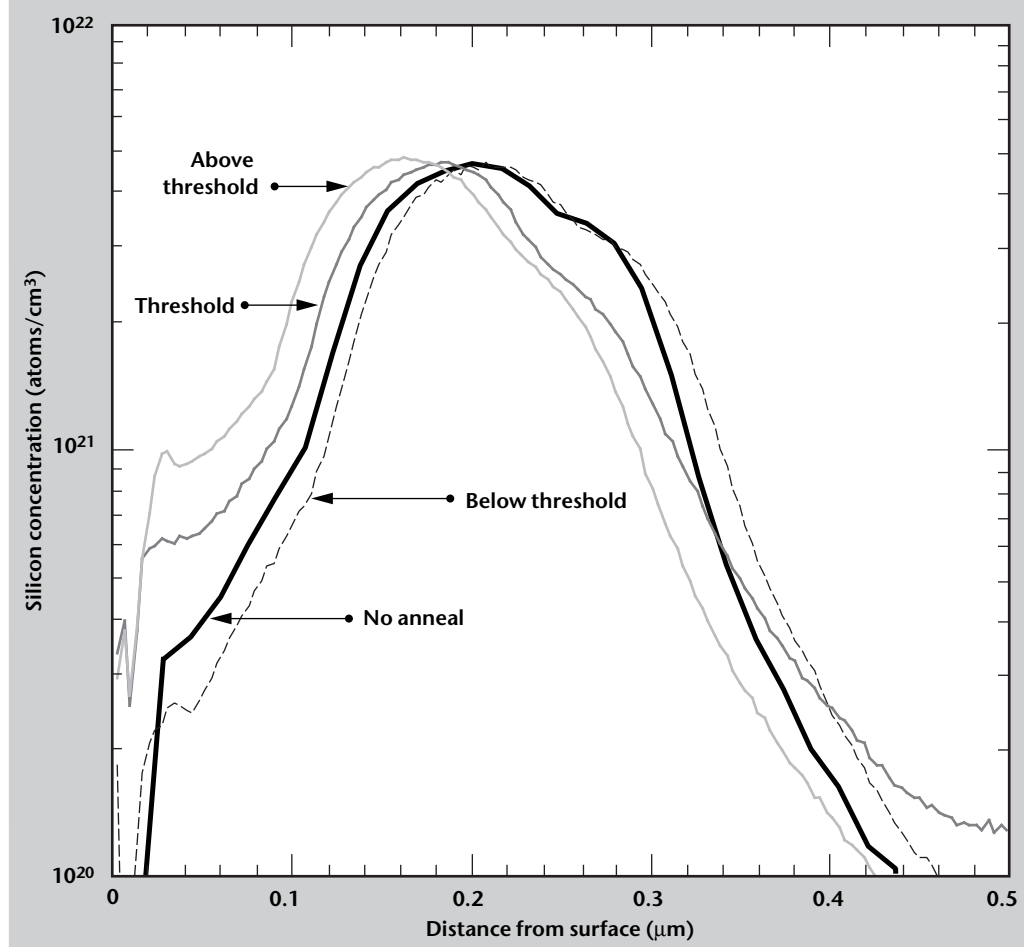


Figure 3. AFM images of GaN surfaces after laser processing. Use of an AlN cap layer prevents GaN decomposition and retains the original surface smoothness.

Figure 4. Secondary ion mass spectroscopy profile of ion-implanted Si in GaN (dose of  $8 \times 10^{16} \text{ cm}^{-2}$  at 150 keV) laser processed at laser fluences above, at, and below threshold. Silicon redistribution is evident at a threshold laser fluence.



The curves obtained for higher fluence are similar to those observed for the undoped films. The TRT measured for the threshold laser pulse has a much shorter melt duration (~120 ns), that is, a shallower melt depth. (Heat flow simulations relating melt duration with melt depths are currently being developed for this material.) This corresponds exactly to what is required for dopant activation. In addition, the surface of the film annealed at threshold is not noticeably roughened. However, atomic force microscope (AFM) analysis indicates that the surface of this sample is covered with Ga droplets, suggesting that some surface decomposition has taken place (**Fig. 3**).

To prevent decomposition of the GaN during laser processing, the surfaces are encapsulated with an aluminum nitride (AlN) capping layer. The AlN was deposited by ion beam sputter deposition (IBS) using an AlN target in a 500-eV N<sub>2</sub>/Ar ion beam. The IR TRT plots and melting thresholds for AlN coated samples were similar to those shown in **Fig 2**. However, a majority of the AlN cap layer was ablated during the laser exposure. AFM analysis of the surface of the AlN-capped sample after laser processing revealed that the surface was intact and that no GaN decomposition had occurred.

GaN films ion-implanted with Si to a dose of  $8 \times 10^{16} \text{ cm}^{-2}$  were coated with a AlN cap layer and then exposed to laser fluences above, at, and below threshold. Secondary ion mass spectroscopy (SIMS) was used to measure the Si profiles of the Si-implanted samples before and after laser processing.

The SIMS data was used to determine the threshold laser fluence at which Si redistribution occurs (**Fig. 4**). As can be seen in **Fig. 4**, the Si surface concentration increases with corresponding increased laser fluence.

## Future Work

We have demonstrated that pulsed laser processing for the activation of dopants in GaN shows compelling promise. However, additional process development is required before this technology can be applied to actual devices. We will vigorously pursue outside funding for the continuation of this work. There are presently opportunities for funding available for GaN microwave power amplifiers through the Innovative Science and Technology Program of the Ballistic Missile Defense Organization.

## References

1. Mishra, U. K., Y. -F. Wu, B. P. Keller, S. Keller, and S. P. Denbaars (1998), "GaN Based Microwave Power HEMTs," *Physics of Semiconductor Devices*, V. Kumar and S. K. Agarwal, Eds., Narosa Publishing House, New Delhi, India, pp. 878-883.
2. Akasaki, I., H. Amano, M. Kito, and K. Hiramatsu (1991), *J. of Luminescence*, **48/49**, p. 666.
3. J. H. Edgar (1994), *Properties of Group III Nitrides, INSPECT, Inst. Electrical Eng.*, London, UK ISBN 0 85296 818 3, p. 192.







# Glass Etching

Harold Ackler and Stefan P. Swierkowski  
*Electronics Engineering Technologies Division*  
*Electronics Engineering*

A radically new type of glass, photostructurable glass, has been evaluated for the first time for suitability for micro-electromechanical (MEMS) structures. The final etch can have an anisotropy ratio of up to 10:1 (20:1 if etched from both sides), and etched features may have steep vertical wall angles of 1 to 4°. These initial results indicate that the glass may be very deeply etched, through the wafer if etched from both sides. However, the trench bottom and sidewall roughness of  $\pm 2 \mu\text{m}$  may preclude some applications with the current level of processing. We have done a multi-parameter etch study on conventional borosilicate glass, since this glass is commonly used in MEMS structures for silicon anodic bonding and glass-to-glass fusion bonding. These types of structures are currently used in major projects at Lawrence Livermore National Laboratory (LLNL). The results have greatly improved the process control to establish undercut ratios, and the control of etch defects, etch-depth uniformity, and etched surface roughness.

## Introduction

Glasses come in many different types and compositions, with vastly different properties and uses. A relatively new photostructurable glass may be patterned into microstructures by exposing regions to be etched with deep UV light. When properly annealed, these regions crystallize into a phase of different composition that etches twenty times faster than the surrounding amorphous material in dilute HF.

The initial surface finish, hidden sub-surface damage, and thermal history of a glass may dramatically affect the formation of microstructures. Many projects at LLNL's Microtechnology Center (MTC) have been patterning borosilicate glass microstructures with varying degrees of success, but the quality of the patterned microstructures has often been severely impaired by the lack of suitable process infrastructure and understanding of the basic causes of defects.

Our recent work on the patterning of large micro-capillary arrays (50 cm long, 100  $\mu\text{m}$  wide and 10 to 100  $\mu\text{m}$  deep) has demonstrated how important certain initial conditions are in determining the quality of the etched pattern. Our evidence shows that non-visible initial scratches and defects play a major role (sometimes disastrous) in the quality and shape of the etched features.

Three glass treatments were studied as a means of eliminating or reducing the effects of such defects. The variation of undercut ratios (side cut/depth) from 1.0 (isotropic) to 2 or greater (anisotropic—fast side etch) is commonly observed and poorly understood. This is attributed, in part, to initial glass conditions, but also to etching technique (for example, etch composition, orientation, convection, reaction rate, reactant diffusion, reaction product removal).

Systematic study of these process parameters is described below.

## Progress

### **Foturan® Photostructurable Glass Processing**

The recommended wavelength for exposure of Foturan® is 290 to 330 nm, where it absorbs moderately. Since it does not absorb at 405 nm (our standard flood/aligner source), the 235-nm lamp was used. Foturan® absorbs strongly at this wavelength, so the depth of the region that is adequately irradiated, and therefore crystallized, was strongly dose-dependent, whereas it is weakly so at the prescribed wavelengths.

Samples were irradiated with 2, 4, 8 and 16 J/cm<sup>2</sup> using a test pattern of lines with spacings



from 20 to 160  $\mu\text{m}$ , with channel spacings equal to channel widths, and large rectangular features 200 to 1000  $\mu\text{m}$  on a side. After annealing, the pieces were etched 10 min (**Fig. 1**). Etch depths measured with a stylus profilometer are summarized in **Table 1**.

Similarly exposed samples were annealed, then cross-sectioned, polished, and etched  $\sim 5$  min to reveal the depth of crystallized material. Crystallization depth vs dose is summarized for the 20- and 40- $\mu\text{m}$  channels in **Table 2**. The large features were crystallized completely through the 0.5-mm wafer for a 16-J/cm<sup>2</sup> dose. Only the 16-J/cm<sup>2</sup> dose appears sufficient to produce crystallization deep enough to fully evaluate possible etch aspect ratios, which are approximately 3:1 with sidewall angles of approximately 6°.

The failure to meet figures specified by the manufacturer are due to the different wavelength used here, which alters the process. The surface roughness was  $\pm 2$   $\mu\text{m}$ . A means of smoothing the surface is yet to be developed. Finally, the CTE of this glass is approximately 8.5 ppm/°C, making it incompatible

with Si and Pyrex. However, it is CTE-matched to Ti, Pt, Al<sub>2</sub>O<sub>3</sub>, and other glasses.

### Process Control for Borosilicate Glasses and Initial Defects

The glass defects responsible for the generation of etch defects are believed to be due to either localized stress caused by mechanical damage, or chemical inhomogeneity. The former should be present only near the surface, and possibly relieved by thermal treatments. One group of Pyrex wafers was polished by a very gentle technique and another annealed. A final group was pre-etched in HF to remove defective material. These groups and another of as-received wafers were patterned and etched with 40- $\mu\text{m}$  channels. The etch defects in channel walls were counted for known lengths of channels and are shown in **Table 3**.

Annealing was not effective in reducing defect rates. Polishing was very effective in that the defect rate was much lower and the defect size was much

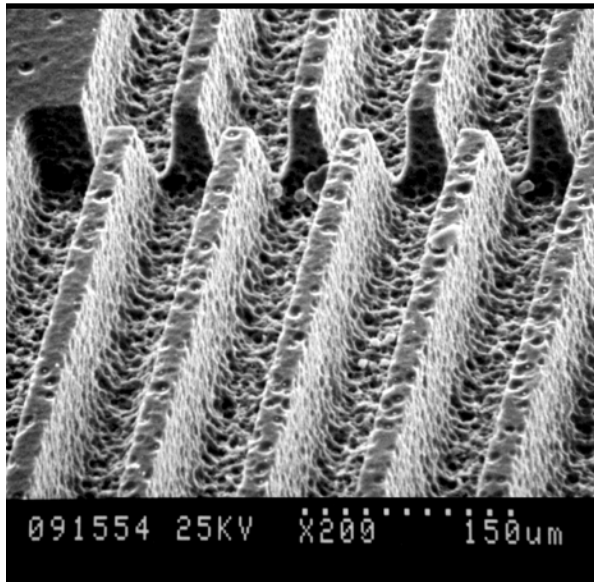


Figure 1. Foturan®, etched 10 min at 8 J/cm<sup>2</sup>.

Table 1. Etch depths ( $\mu\text{m}$ ).

Dose (J/cm <sup>2</sup> )	Feature width ( $\mu\text{m}$ )				
	40	80	120	160	1000
2	20	30			25
4	20		35		35
8		45		65	65
16		50		65	75

Table 2. Crystallization depths ( $\mu\text{m}$ ).

Dose (J/cm <sup>2</sup> )	Feature width ( $\mu\text{m}$ )	
	20	40
2	24.5	27.5
4	47.5	37.5
8	100	
16		164

Table 3. Defect rates in treated Pyrex wafers.

Wafer treatment	Average (defects/cm)	Standard deviation (defects/cm)	cm of 40- $\mu\text{m}$ channel
As-received	47	26	$\sim 6$
Annealed	35	18.6	$\sim 6.5$
Polished	6.8	2.5	$\sim 6.5$
Pre-etched	0.23	0.46	$\sim 4$

smaller. However, this method costs approximately \$200/wafer through a vendor. The pre-etch was remarkable at reducing defect rates to almost zero, with very small defects when observed. This process takes an extra 15 min; however, it leaves pits scattered over the entire surface, which are at most 250 nm deep. The effects of those pits that intersect channel edges on device performance have not been fully considered. They might be sealed up during bonding; however, this has not been completely evaluated.

A large set of parametric etch experiments were carried out on borosilicate (Pyrex) glass using Cr-Au as the etch mask with a varying grating pattern<sup>1</sup>. A few selected results are discussed. The quality of etching is strongly dependent on the etch composition, concentration, mask composition and definition, agitation, and prior history of the glass surface. Data from a frequently used (60 min duration/21 °C) etch is shown in **Fig. 2**.

These etch experiments show that the absolute roughness (vs normalized with depth) for **Fig. 2** is about 10 to 40 nm. This is true over a wide range of concentrations and depths, and to some extent, composition. Roughness can be dramatically worse if the surface of the glass is damaged, even with non-visible defects, especially scratches. For very high etch rates, the reaction products can't be removed quickly enough, resulting in very poor etch definition and roughness.

In **Fig. 2**, the absolute value of roughness remained approximately constant at ~30 nm as the HF concentration increased. However, the higher HF concentrations more rapidly remove the patterned field photoresist (6  $\mu\text{m}$  thick), which is left over the Cr/Au etch mask (1  $\mu\text{m}$  thick) as additional support.

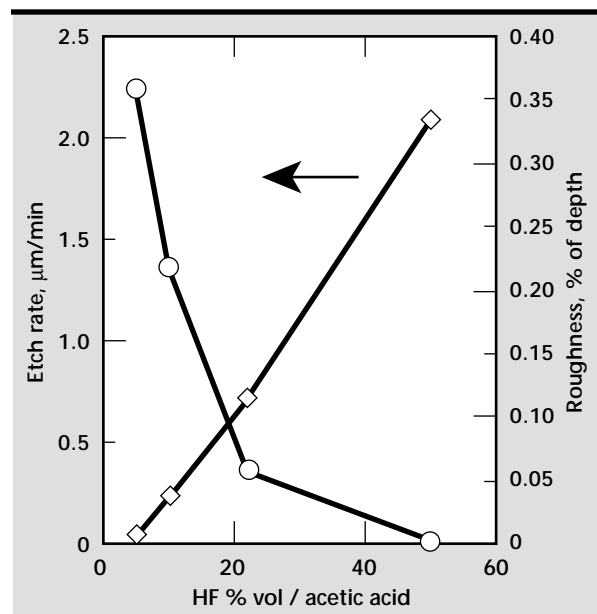


Figure 2. Etch parameters for borosilicate glass.

Since this etch is approximately isotropic, it undercuts the Cr/Au/photoresist mask significantly.

Uniform etch agitation is essential for uniform depths. The higher agitation needs a stronger mask and the higher the agitation, the more the mask is undercut. For etch times much longer than 60 min in the 22%-HF etch, the mask starts to seriously degrade with pinholes or cracking. The 22%-HF etch is a compromise between etch rate, roughness, and mask degradation.

A typical etch result is shown in **Fig. 3**. The total mask undercut is about the same as the depth, that is, 40  $\mu\text{m}$ . The etch rate is reduced in the corner underneath the mask near the surface. The reaction rate and product removal is reduced here by limited convection, so the glass is locally etched anisotropically and yields a final glass undercut of 5  $\mu\text{m}$ . The lateral definition of the glass edge appears to significantly replicate the roughness of the Cr pattern after it is etched. Care must be taken to not over-etch the Cr, as it will undercut the Au and result in more jagged Cr edges.

Etch studies taken with small (7 cm) test pieces have yielded significant differences in uniformity compared with very large rectangular (15 cm  $\times$  58 cm) plates. The etch-volume to surface-area-being-etched ratio, combined with the detailed etch flow patterns during agitation, appears to be very important.

For etching small samples placed vertically along the wall of the etch beaker we have etch rates of about 0.75  $\mu\text{m}/\text{min}$ —independent of zero, medium, or high-spin speeds. For etching small samples placed horizontally along the bottom of the etch beaker, we have etch rates of about 0.89  $\mu\text{m}/\text{min}$ —

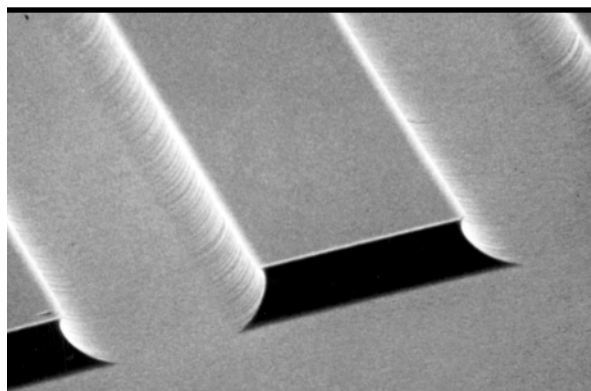


Figure 3. Etched channels in borosilicate glass, 40  $\mu\text{m}$  deep, on a 250- $\mu\text{m}$  pitch. The 5- $\mu\text{m}$  undercut is key to forming a rounded channel.

independent of zero, medium, or high-spin speeds. The etch uniformity across these small samples is very good—less than 2%.

For large rectangular plates with a longitudinal etch agitation, the etch uniformity of the initial experiments could be higher, lower, or in the middle by 25%, depending on the agitation conditions. The lateral etch uniformity was very good—less than 2%. By optimizing the agitation conditions for large plates, overall longitudinal uniformity of etch depth of <4% has been achieved simultaneously with excellent lateral uniformity.

Using the baseline etch composition of HF 22% vol/acetic acid at 21 °C, the etch rate was reduced to 2/3 its value with a temperature of 5 °C, while the surface roughness may have been reduced slightly. The surface roughness measurements were highly variable since they were not averaged much at all. The exception is the roughness of the glass before processing, and on the unetched surface after processing, and this value was consistently between 0.8 and 1.3 nm.

Trying a few experiments with other HF-type etches including nitric acid, water, and acetic acid with small amount of surfactant did not yield any dramatic changes in etch rate or surface roughness, except that in some cases the etch mask was attacked more rapidly. Attempts to use sputtered Mo as an etch mask failed because of persistent pinholes and very high stresses in the film that made it crack during etching. Cr/Au/photoresist has worked very well as a mask material: e-beam Cr (30 nm) gives excellent adhesion to the glass and the subsequent Au. Au (1  $\mu\text{m}$ ) gives a thick, compliant, low-stress layer that is highly etch-resistant. The top layer of photoresist (6  $\mu\text{m}$ ) helps to mechanically support the Au as the etch proceeds to undercut the metal mask with significant etch convection

taking place. This type of coating is amenable to low particulate defects and very large substrates. This masking layer can even be blown dry with nitrogen for intermediate depth inspection, followed by continued etching.

## Future Work


Continued study of Foturan<sup>®</sup> processing will include increasing etch aspect ratios and etch uniformity, and reducing surface roughness. The effect of surface pits generated during pre-etching of Pyrex wafers on device performance and potentially sealing them during bonding will be studied. The etching of borosilicate glass seems to yield an initial surface roughness of about 20 nm that doesn't get rapidly worse with increasing etch depth. The factors controlling this roughness are not well understood.

The inhomogeneities and impurities in the glass have not been characterized and should be studied further. For etch depths much more than about 75  $\mu\text{m}$ , improved mask materials or etch compositions will be needed.

## Acknowledgments

We gratefully acknowledge the assistance of D. Hilken and L. Tarte with the lithography and etching. Support for the microchannel array portion of the genome sequencing project at LLNL is appreciated.

## Reference

1. Swierkowski, S. (1997), "Large Area Lithography," Engineering Research, Development and Technology, Lawrence Livermore National Laboratory, Livermore, California (UCRL-ID-125472), p. 3-23. 



# Micro-Electromechanical Systems — Foundry Interface

**Michael D. Pocha**

*Electronics Engineering Technologies Division*

*Electronics Engineering*

The goal of this project was to establish a working interface between Lawrence Livermore National Laboratory (LLNL) and one or more micro-electromechanical systems (MEMS) foundries so that we could provide LLNL programs with a one-stop service for research and development of custom microstructures. Early in the project we found that traditional foundries make most of their money from volume manufacturing and are, therefore, not interested in the small-scale work that we need. Two small custom fabrication companies were identified, one for silicon MEMS and the other for glass/ceramic component fabrication. The silicon fabrication company proved excellent, and we are beginning to use their services for programmatic projects. The glass/ceramic fabrication company could not deliver the quality of components we need, however, and we are going elsewhere for those components. This project was extremely useful in that we were able to evaluate the capability of two companies, narrowed down from a much wider field. Also, we can now provide the components needed by our programmatic customers with confidence.

## Introduction

The Microtechnology Center at LLNL is primarily a research facility for design and development of microstructures and microsystems. We typically perform the research needed to develop novel microstructures for a variety of programmatic and external customers. We generally build prototypes of the devices and systems we develop, but are not equipped to provide significant production quantities. We have several customers, however, who would like small-scale production quantities of devices. Recently, several commercial companies have advertised that they provide foundry service for MEMS, just as foundries have existed for custom integrated circuits for several years.

Most of the customers who would like production quantities are working on tight budgets and schedules, and cannot afford the cost and time delay for us to establish the interface and learn how to work with foundries. A small investment in establishing this interface and learning how to work with foundries will make it much more attractive and efficient for the programmatic customers to get the services they need.

Some foundries have low-cost multi-project fabrication services if one can use their standard process. These have a well-defined interface and are easy to use. They were not addressed by this project. We were interested in establishing a process for custom fabrication that is more general and able to satisfy a broader set of our needs. We began this project by contacting three possible foundries for custom silicon fabrication. They were identified from ads in trade journals, personal contacts, and internet searches.

All three foundries told us essentially that they can only provide large volume fabrication to be profitable. Microelectronics Center of North Carolina (MCNC) gave us a quote for a small run, but it was approximately five times higher than our costs to fabricate the same component in-house. We turned, then, to small custom fabrication companies who did not consider themselves as “foundries” *per se* but were more willing to consider the small production runs that we need. There were three in the San Francisco Bay Area whom we identified primarily from personal contacts established over the years. One of these, Nanostructures Inc., has proved to be able to provide the quality and quantities we need at

reasonable cost (comparable to fabricating in-house). We have already used their services for one programmatic customer with very favorable results and are beginning to perform another run for a second customer.

In a second technology area, we are increasingly interested in fabricating components in non-semiconductor materials like plastic, glass, and ceramic. Here we identified a company, Applied Ceramics in Fremont, California, that was willing to do glass and ceramic cutting more quickly and at less cost than others. Applied Ceramics had the potential not only to perform precision drilling and cutting of substrates, but also to provide substrates of many different materials. Unfortunately, they were not able to deliver the quality of material needed. But, we found that out without having committed any of our customers' funds. This project has been very beneficial to LLNL and will save the programs considerable cost and time in the future. We highly recommend other such projects for technology-base support.

## Progress

As mentioned earlier, some foundries offer a multi-project chip where several different designs from several customers are all fabricated on a single silicon wafer, thus, lowering the cost to each customer. MCNC, for example, offers such a process for three-layer polysilicon-surface micromachined components. If you can make your design fit their standard process, you can purchase custom MEMS components for as low as \$2,900 per run. They also have other standard processes to choose from. We have used this option. However, only about 10% of our structures can be designed within the constraints of the standard processes. We need a procedure for procuring components requiring a larger set of fabrication technologies.

An example we chose as representative of many of the components we need to fabricate is the silicon optical microbench. These chips need to have 1) pedestals or wells etched into the silicon surface several tens of micrometers deep; 2) polysilicon deposited and doped to obtain the correct resistivity for electrically activated heaters for melting solder; and 3) metal interconnects patterned on both levels of the steps in the silicon surface created during the pedestal/well etch. This set of steps encompasses the majority of silicon micromechanical components we design and build.

We are also often designing and building components out of materials other than silicon (glass, plastic, ceramic). Here, the primary new process step is the etching and drilling of holes in these materials. Patterning of plastic is a very broad and complex subject which was beyond the scope of this project.

Two companies that we know of provide custom patterning of glass and ceramic: Bullen Ultrasonics, Inc., in Eaton, Ohio and Applied Ceramics in Fremont, California. We have used Bullen Ultrasonics in the past, and so chose to try out Applied Ceramics, geographically closer to LLNL and offering lower cost service.

**Table 1** below summarizes the results of our discussions and interactions with the companies we contacted.

In summary, after our extensive search, we found one company that was able and willing to fabricate the silicon microbenches and another company to evaluate for etching and drilling of glass and ceramic substrates. The silicon microbench fabrication was more successful than the glass and ceramic substrate fabrication.

Nanostructures Inc. delivered silicon microbenches, which we were able to deliver to an LLNL program. Our customer was happy to get free parts, but more importantly, pleased that he can now purchase microbenches, in quantity, at a fixed cost. We are in the process of making modifications to the design for the next generation of microbenches to be purchased from Nanostructures Inc.

We have also just placed an order for PCR Thermalcyclers, another component that requires the same silicon etching and polysilicon resistor formation process. We anticipate out-sourcing these well-defined and relatively simple designs, ultimately saving LLNL significantly more than the cost of this project.

Our experience with Applied Ceramics was not as successful. We contracted with them to deliver ten polished  $\text{Al}_2\text{O}_3$  ceramic wafers with holes drilled in a prescribed pattern, and to drill a similar pattern of holes in Pyrex wafers that we supplied to them. The ceramic wafers were delivered with surfaces that were too rough for our applications and the holes, although placed correctly, had very rough and chipped edges. Also, the glass wafers had severely chipped holes which are unacceptable for our applications. We will, therefore, continue to get glass and ceramic substrates from the more expensive supplier, Bullen Ultrasonics, Inc.

Table 1. Summary of foundry research.

<b>Silicon MEMS foundries</b>	
Microelectronics Center of N. Carolina 3021 Cornwallis Road Research Triangle Pk., NC 27709 (919) 248-1800	(MUMPS) Multi-project run. Bid - \$2900 for designs that use standard three-level polysilicon-surface micromachine processing.  Full custom processing such as the silicon microbench; only interested if production lots are sufficiently large to be profitable to produce. Bid - \$53,000.
Standard Microsystems Corp. 35 Marcus Boulevard Hauppauge, NY 11788 (516) 435-6961	Set up for volume production of silicon components; only interested at the 100 to 1000 parts per week level. No bid.
MEMStek Products, LLC 2111 SE Columbia Way Suite 120 Vancouver, WA 98661	Specialize in microfluidic delivery systems such as pumps and valves. Not interested in general MEMS. No bid.
<b>Small custom fabrication</b>	
MicroFlow Inc. 6701 Sierra Court Dublin, CA 94568 (925) 828-9650	Initially interested in bidding on our project, but were just acquired by a large custom house, Input/Output Inc., Houston, Texas. While we were in discussions, the new management made the decision that this project was too small to warrant further effort, so discussions ended. No bid.
TiNi Alloy Company 1621 Neptune Drive San Leandro, CA 94577 (510) 483-9676	Specialize in shape memory alloy actuated devices using Ti and Ni alloys. Had some initial interest in silicon fabrication to expand their capability, but while we were discussing our requirements, decided to concentrate on their core business. No bid.
Nanostuctures Inc. 3070 Lawrence Expressway Santa Clara, CA 95051 (408) 733-4345	Interested in our job. Bid \$9500. Successfully fabricated microbenches.
<b>Non-silicon fabrication</b>	
Applied Ceramics 850 Corporate Way Fremont, CA 94539 (510) 249-9700	Delivered glass and ceramic substrates with holes in specified locations. Bid - \$4150. Fabricated parts, but unacceptable quality.


Even this negative experience was useful because it confirmed that we were getting our glass and ceramic substrates from the most cost effective source.

### **Future Work**

This was an excellent technology-base project. We recommend that each year a small amount of technology-base funding be set aside for the identification and evaluation of vendors to supply well-defined,

non-research components. We can concentrate our more expensive resources (people and equipment) on the research we do best, but still supply our customers who need them a significant quantity of production components.

### **Acknowledgment**

The author would like to thank H. Ackler at LLNL for conducting the non-silicon fabrication part of this project. 



# Hydrogel-Actuated Implantable Sensor

**Amy W. Wang, Abraham P. Lee, and Charles F. McConaghy**

*Electronics Engineering Technologies Division*

*Electronics Engineering*

**Christopher B. Darrow, Stephen M. Lane,  
and Aleksandr Gilman**

*Medical Technologies Program*

**Joe H. Satcher, Jr.**

*Chemical Sciences Division*

*Chemistry and Materials Science*

With this project we seek to demonstrate hydrogel-based transduction and telemetry technologies that could lead to a new class of implanted medical sensor devices. An implanted sensor is useful for any patient who must monitor a particular blood analyte and, thus, requires frequent extraction of blood samples. Examples include electrolyte and pH measurements (potassium, sodium, calcium) for many chronically ill patients, urea and potassium for dialysis patients, immuno-suppressant drugs for transplant and AIDS patients, anti-coagulants for many heart and stroke patients, and glucose for diabetic patients. We envision a wristwatch-sized, externally-powered component worn by the patient, which interrogates a passive, implantable element.

## Introduction

Hydrogels are a class of polymers that have a high capacity for water absorption. Typical mass increases for the hydrated state of such polymers, for example, poly-hemas (PHEMAs), may be 10 to 100 times, and swelling volume ratios of up to 30% can be achieved. We are interested in suitably modified polymers that, in the hydrated state, exhibit reversible swelling in response to a change in pH, osmolarity, temperature, pressure, or the concentration of some analyte of interest. Enzymes can be embedded in the hydrogel to create specificity to a given analyte.

Currently, hydrogels are commercially used in absorbents, thickeners, dilators, and as osmotic pumps. However, few researchers have used hydrogels as an actuator for micromechanical structures. With the swelling volume achievable by these polymers, significant mechanical work may be accomplished.

## Progress

We have demonstrated a micro-electromechanical system (MEMS) sensor that is sensitive to the concentration of an ionic solution, and a prototype passive resonant circuit that can be used for remote interrogation of the device. The sensor is actuated by a biocompatible PHEMA hydrogel that swells or shrinks in response to variations in concentration of an ionic solution. It consists of a silicon cell that encapsulates the hydrogel between a deformable membrane and a liquid-permeable mesh chip (**Fig. 1**).

As the hydrogel changes dimensionally in response to an analyte in solution, it flexes a deformable, conducting membrane that forms one plate of a parallel plate capacitor. The capacitive variation can be monitored by incorporating the hydrogel capacitor into a resonant LC circuit, such that a change in analyte concentration is reflected by a shift in resonant frequency of the circuit.



This design can be used in an implantable system in which a signal is sent transdermally, sweeping a range of frequencies to interrogate the implanted device and detect variations in resonant frequency. The signal can be transmitted or reflected back to the interrogating circuit, which is mounted at the skin surface in a readout package similar to a wristwatch.

### Silicon Cell

The silicon cell encapsulating the hydrogel consists of two silicon chips bonded together. One wall of the cell is a deformable membrane formed from a 2- $\mu\text{m}$ -thick biocompatible NiTi-based film sputtered on a 0.5- $\mu\text{m}$  silicon nitride membrane. Nitride membranes are formed by silicon etching in potassium hydroxide (KOH). We found that NiTi-based membranes are preferable to gold-coated silicon nitride membranes in durability, since contraction of the polymer during drying results in breakage of the gold-nitride membranes. The NiTi-based membranes were used successfully and found to be quite robust.

The opposite wall of the cell consists of a rigid mesh made up of a 50- $\mu\text{m}$ -thick silicon chip with 100- to 200- $\mu\text{m}$ -size holes etched through its thickness. The mesh allows exposure of the hydrogel to the ambient analyte solution, while constraining the hydrogel. Fabrication of the mesh involves double-sided exposure of the mesh area and mesh holes on a silicon wafer, then simultaneous KOH silicon etching from both sides of the wafer, thinning it down to a thickness of 50  $\mu\text{m}$  and etching through the holes.

### Hydrogel Testing

Both uncross-linked and cross-linked PHEMA hydrogels were tested for swelling in response to the

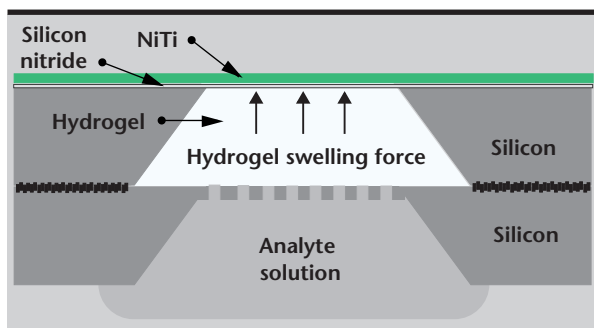


**Figure 1.** Diagram of hydrogel-actuated silicon MEMS cell. Hydrogel swelling in response to an analyte causes deflection of a conductive membrane and a resultant change in capacitance of a parallel plate capacitor.

concentration of a calcium nitrate solution. Uncross-linked PHEMA gels were dissolved in methanol, pipetted into the silicon cell in liquid form, then dried before rehydration in water.

Cross-linked gels were dried in a nitrogen environment before rehydration. Gel swelling was observed for both types of gels, but cross-linked polymers exhibited more lateral swelling, rather than out-of-plane swelling that would displace the flexible membrane.

Uncross-linked PHEMA displayed good out-of-plane displacement, and increased swelling was observed with increasing salt concentration.

Optical membrane displacement measurements showed 4  $\mu\text{m}$ , 20  $\mu\text{m}$ , and 30  $\mu\text{m}$  peak displacements for calcium nitrate concentrations of 0.5 M, 1 M, and 3 M, respectively. **Figure 2** shows an example of an optical measurement of membrane displacement ( $\sim 30 \mu\text{m}$ ) due to polymer swelling. At high salt concentration, the polymer began to extrude through the holes of the mesh chip due to “untangling” of the polymer strands. A thin layer of “stiffer” polymer used between the PHEMA and the mesh chip reduced the amount of extrusion. We have yet to determine hysteresis effects of the hydrogel.

### Interrogation Circuitry

We have also built a resonant antenna circuit in which an inductor coil remotely probes a passive LC circuit. A network analyzer was used to sweep the interrogation frequency and measure the power reflected back through the inductor to indicate the resonant frequency (minimum reflected power) as shown in **Fig. 3**. We were able to interrogate the passive circuit with the inductor 5 mm away from the circuit, a distance that is sufficient for a sensor implanted directly beneath the skin. From optical displacement measurements, we predicted capacitive

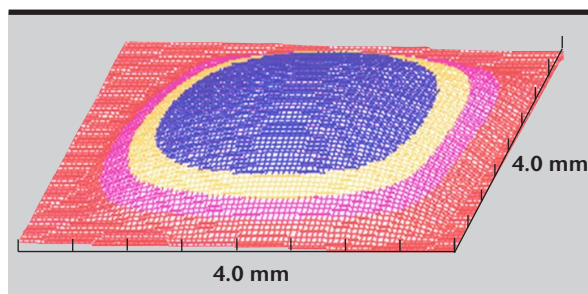


**Figure 2.** Optical measurement of membrane deflection due to hydrogel swelling.

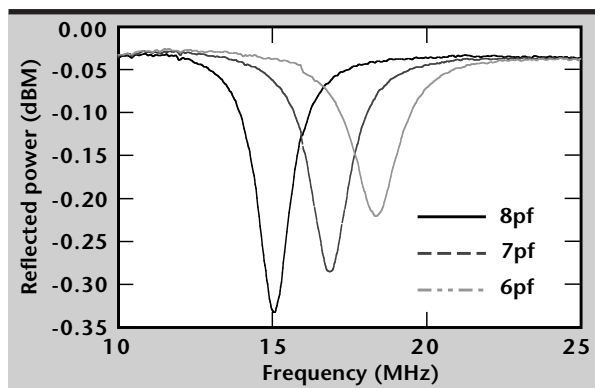



Figure 3. Reflected power from the resonant circuit. Resonance is indicated by minimum reflected power. Capacitive variations of 1 pF result in approximately a 1.5-MHz shift in an 18-MHz resonance frequency.

changes on the order of 1 pF due to polymer swelling. Using our antenna circuit, we were able to detect 1-MHz shifts in an 18-MHz resonant peak for incremental changes of 1 pF (Fig. 3).

In summary, we have demonstrated that significant shifts in resonant frequency can be observed as a result of hydrogel swelling, and that it is feasible to implant a passive circuit and use telemetry to interrogate the implanted element.

## Acknowledgments

The authors gratefully acknowledge H. Ackler and P. Krulevitch for their ideas, discussion, and processing advice, and P. Ramsey for the deposition of the NiTi films. 



# ambda Connect: Multi-Wavelength Technologies for Ultrascale Computing

**Robert J. Deri, Michael C. Larson, and Michael D. Pocha**

*Electronics Engineering Technologies Division  
Electronics Engineering*

**Mark E. Lowry**

*Defense and Nuclear Technologies*

Byte-wide, multi-wavelength optical interconnects can substantially improve the performance of the system interconnects used in ultrascale computing platforms ("supercomputers"), leading to substantial improvements in overall system performance for applications that require global communications within the supercomputer. This year, we have developed the first generation of optical hardware required for such interconnects: byte-wide multi-wavelength transmitters and wavelength filters. The performance of these prototypes demonstrates the viability of our approach.

## Introduction

Ultrascale computing—the integration of large numbers of processors into a single, highly capable multi-processor system—is currently of great interest in several government programs. These systems contain 100s to upwards of 1000 CPUs, to attain computing capabilities from 100 GFLOPS to 100 TFLOPS and beyond.

The provision of fast data communications within such systems poses a significant challenge. Effective communication is currently hampered by the bandwidth, latency, and congestion characteristics of the electronic fabric used to interconnect the many system-processing and memory elements. This communications bottleneck can substantially degrade computational performance, significantly complicate programmability, and cause inefficient use of costly memory resources.

The recent emergence of byte-wide optical interconnects, which use linear arrays of multi-mode optical fibers in a ribbon cable assembly, has substantially improved the cost and performance of Gbyte/s point-to-point communications. To fully leverage this technology, however, the latency and congestion issues with distributed electronic switching must be overcome.

We have recently proposed source-routed switching in the optical domain using a wavelength-switching mechanism. We have shown that this approach can yield highly capable switches that support 100s of

Gbyte/s ports and yield minimal internal congestion and latency. Instruction-level simulation has demonstrated the advantages of this approach.<sup>1</sup>

To implement this multi-wavelength optical interconnect requires the addition of multi-wavelength capability to the existing byte-wide optical interconnect. The required components, which include optical transmitters capable of fast wavelength tuning, and fixed optical filters differ substantially from existing telecommunications fiber optics. All components must be compatible with existing multi-mode fiber ribbon cables, and provide compact form factors suitable for populating electronics boards.

This project aims at developing prototypes of these components, to investigate the feasibility of implementing byte-wide, multi-wavelength optical interconnects for ultrascale computers.

## Progress

### Multi-Wavelength Transmitters

We have developed prototype modules with the capability of transmitting on any of two or four selectable wavelengths. The module wavelength is selected by directing current into different lasers, each laser emitting at a different wavelength, so that current switching is used to provide fast wavelength switching on a timescale of the laser modulation bandwidth (1 to 2 ns switch time). Each module contains one linear array of 10 laser diodes for each

wavelength. Each array element can be independently addressed (modulated) by a current drive, so that the module can transmit 10 independent data streams comprising the 8 bits in an electronic data word of 1 byte capacity, plus clock and framing.

Our modules use arrays of vertical cavity, surface-emitting lasers (VCSELs), which we have fabricated from AlGaAs semiconductor layers grown by molecular beam epitaxy. Our VCSEL design uses an oxidized AlAs layer to control the “active region” of the laser which is pumped by the applied current drive, to achieve lasing thresholds of 2 mA for devices of 5 to 15  $\mu\text{m}$  oxide aperture.

The VCSELs are sized to emit in multiple transverse modes (1.5 nm spectral extent), to minimize speckle noise during multimode fiber transmission. These devices provide milliwatts of optical power when pumped with <10 mA at  $\leq 3$  V, conditions compatible with conventional CMOS electronic drive electronics. **Figure 1a** shows a typical VCSEL optical output characteristic as a function of drive current.

We use a separate VCSEL array chip for each selectable wavelength in our modules, with each chip originating from a separately processed AlGaAs wafer. This approach enables us to select an arbitrary spacing between system wavelengths, and enables the system wavelengths to span a very wide spectral range (many 10s of nanometers). This is attractive because it allows a moderate channel separation (8 to 10 nm) that minimizes issues associated with wavelength registration, uniformity, and drift between different photonic components within the interconnect.

This year, we demonstrated a dual-wavelength transmitter module that can launch light of either 815 or 830 nm into all 12 fibers in a ribbon cable. The optical signals are independently addressable,

and originate from two VCSEL chips with approximately 6  $\mu\text{m}$  oxide apertures.

**Figure 1b** shows our ceramic pin-grid-array (cPGA) module, which contains two laser chips. Each laser chip provides a different wavelength, and the emitters from both chips are coupled into a single fiber using passive optical alignment to a standard ribbon cable.

The dual-wavelength module exhibits good performance, as shown by the optical spectrum and 400 Mbit/s eye pattern of **Fig. 2**. The spectrum shows simultaneous emission into a single fiber from two wavelengths, with signal-to-noise ratios of 30 dB. All laser elements are functional, and deliver >2 mW of optical power into the fiber cable.

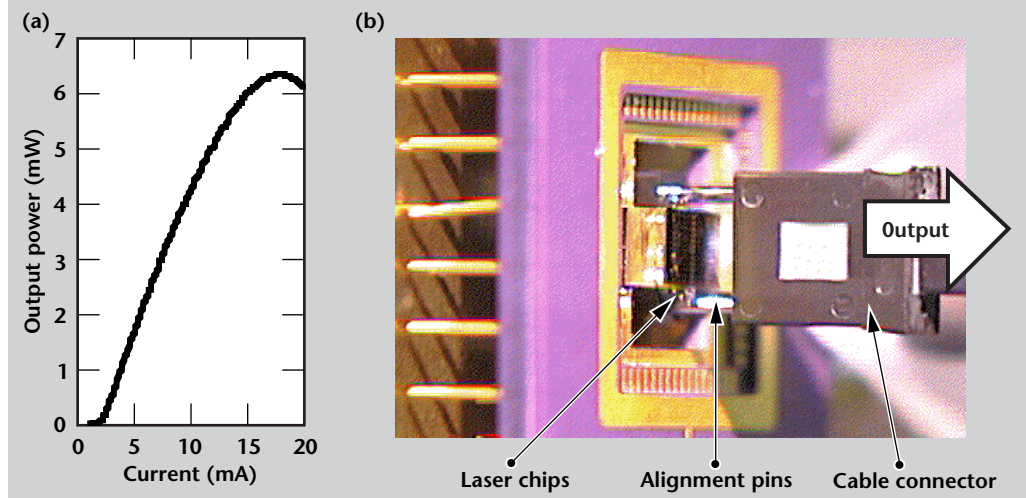
We have verified that the packaged lasers are suitable for high speed operation by observing their performance under high-speed modulation.

Our cPGA package exhibits resonance-free performance to 300 MHz when mounted with appropriate external impedance matching resistors. We anticipate that the module frequency response can be extended to the VCSEL device limit of several GHz by using suitable internal terminations and driver electronics, and possibly by transitioning to a higher-speed ceramic package.

We evaluated our module's transmission performance in a link using a commercial 400 Mbit/s receiver which performs some reshaping. The resulting eye pattern (**Fig. 2**) exhibits an open eye and measured bit error rates below  $10^{-14}$  at 400 Mbit/s per fiber for a pseudo-random bit stream of sequence  $2^{23}-1$  bits.

We extended our optical packaging approach to a four-wavelength transmitter module by using a proprietary, optical superstrate assembly. This assembly combines optical signals from four VCSEL

**Figure 1. Dual-wavelength transmitter module:** (a) light output vs drive current for VCSEL device (unpackaged); (b) overall ceramic PGA module, showing alignment to a fiber ribbon cable. The cable connector is 6.4 mm wide.



arrays, operating at wavelengths 823, 843, 971, and 986 nm. **Figure 3** shows the complete four-wavelength module in its cPGA package, and its output spectrum when all wavelengths are simultaneously activated. The module uses a similar guide pin approach for connecting to ribbon cable assemblies.

### Byte-Wide Filter Modules

We have developed optical filter modules based on the packaging of thin-film interference filters within a housing comprised of ribbon cable connector

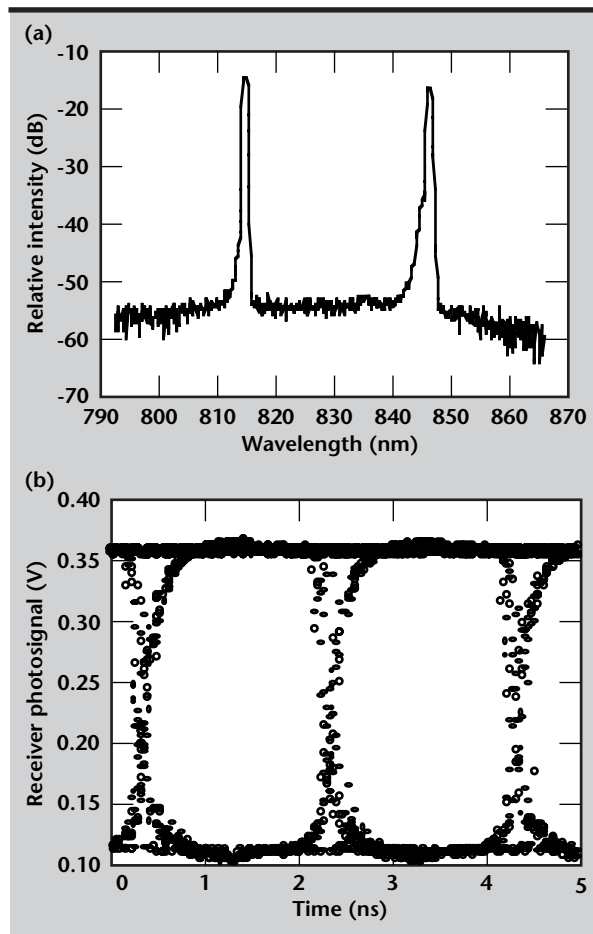


Figure 2. Dual-wavelength module spectrum (a), and high-speed signalling performance (eye diagram)(b). Note that the spectrum is displayed on a logarithmic (decibel) scale.

ferrules.<sup>2</sup> The advantages of this approach are that 1) the module is assembled primarily by passive alignment using interlocking guide pins, and 2) the module automatically mates to ribbon cable connectors.

This year, we extended our filter approach to narrow band filters and to improved transmission characteristics for enhanced system channel spacing and wavelength tolerances.

**Table 1** summarizes the performance of modules using single-cavity Fabry-Perot filters. The data show that acceptable insertion loss can be achieved for filter bandwidths as small as 4 nm. Modules with the broader (14 nm) passband have been cascaded in series to improve cross-talk suppression and to achieve somewhat narrower passbands. The modules exhibit a fiber-to-fiber wavelength uniformity ( $\pm 1$  nm) sufficient for channel spacings of several nanometers.

Filter modules with a flatter top and sharper skirts than are obtainable from the Lorentzian line-shape associated with single cavity designs are valuable, because they improve system tolerances to variations and drifts in the wavelengths of individual transmitter and filter modules, and enable tighter spacing of wavelength channels.

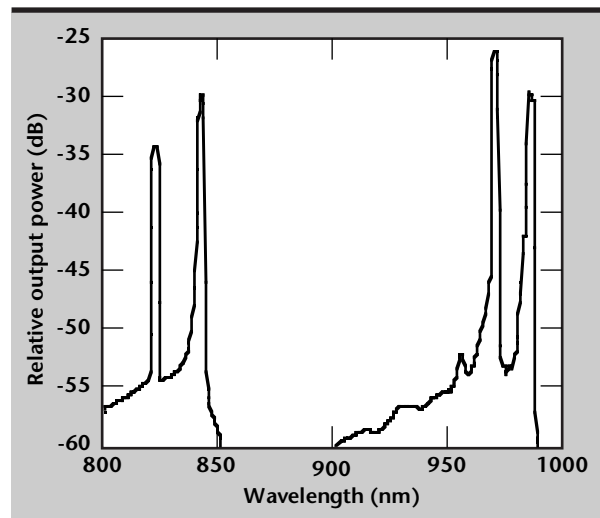


Figure 3. Output spectrum of four-wavelength module in cPGA. Note that the spectrum is displayed on a logarithmic (decibel) scale.

Table 1. Single cavity Fabry-Perot filter characteristics.

Filter bandwidth	14 nm	4 nm
Number of layers in Bragg reflector	12	20
Packaged insertion loss (dB) average, <best>	1.5 <0.8>	2.7 <1.9>
Unpackaged insertion loss (dB) (collimated beam)	0.76	1.1
Cross-talk suppression (dB)	-11 (no cascade)	-19

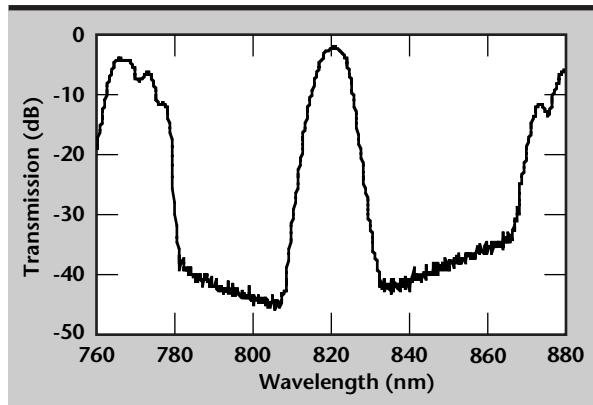


Figure 4. Transmission response of multi-cavity filter module.

We have demonstrated such a filter module, based on a multi-cavity interference filter design. Its response (**Fig. 4**) shows a flatter top and substantially sharper filter skirts than are achievable with single cavity devices, and exhibits cross-talk suppression better than 30 dB. Filter skirt sharpness can be quantified by the ratio of the filter's 3 dB bandwidth to 20 dB bandwidth. This ratio is 0.48 for the device of **Fig. 4**, three times sharper than our single cavity devices. This device is suitable for channels spaced 8 to 10 nm apart, and provides a 5-nm tolerance window for component wavelength variations (at 1 dB excess loss).

## Future Work

These results demonstrate the feasibility of high-performance optical components for byte-wide, multi-wavelength optical interconnects, showing that compact, high-performance transmitter and filter modules can be realized for systems using four wavelength channels.

Our goal for next year is to demonstrate components enabling systems with higher wavelength count, since earlier simulations showed that eight system wavelengths are required for several interesting multiprocessing applications.<sup>2</sup> We also intend to develop additional passive routing devices for byte-wide interconnects, including N-to-N star broadcast components.

## Acknowledgments

This project has benefited substantially from the efforts of M. Emanuel, H. Garrett, W. Goward, R. Patel, and H. Petersen of LLNL, and from contributions by Prof. C. Gu (University of California, Santa Cruz), and Prof. R. F. Drayton (University of Minnesota).

## References

1. De Groot, A. J., and R. J. Deri (1996), *Proc. Third Intl. Conf. Massively Parallel Processing using Optical Interconnections*, IEEE, October.
2. Deri, R. J., and S. Gemelos (1998), "Simple fabrication of WDM filters for byte-wide, multimode cable interconnects," *Integrated Photonics Research Conf.*, Victoria, Canada, April.

